
Towards Nonlinear Disentanglement in Natural Data with Temporal Sparse Coding

David Klindt*

University of Tübingen
klindt.david@gmail.com

Lukas Schott*

University of Tübingen
lukas.schott@bethgelab.org

Yash Sharma*

University of Tübingen
yash.sharma@bethgelab.org

Ivan Ustyuzhaninov

University of Tübingen
ivan.ustyuzhaninov@bethgelab.org

Wieland Brendel

University of Tübingen
wieland.brendel@bethgelab.org

Matthias Bethge[†]

University of Tübingen
matthias.bethge@bethgelab.org

Dylan Paiton[†]

University of Tübingen
dylan.paiton@bethgelab.org

Abstract

We construct an unsupervised learning model that achieves nonlinear disentanglement of underlying factors of variation in naturalistic videos. Previous work suggests that representations can be disentangled if all but a few factors in the environment stay constant at any point in time. As a result, algorithms proposed for this problem have only been tested on carefully constructed datasets with this exact property, leaving it unclear whether they will transfer to natural scenes. Here we provide evidence that objects in segmented natural movies undergo transitions that are typically small in magnitude with occasional large jumps, which is characteristic of a temporally sparse distribution. We leverage this finding and present SlowVAE, a model for unsupervised representation learning that uses a sparse prior on temporally adjacent observations to disentangle generative factors without any assumptions on the number of changing factors. We provide a proof of identifiability and show that the model reliably learns disentangled representations on several established benchmark datasets, often surpassing the current state-of-the-art. We additionally demonstrate transferability towards video datasets with natural dynamics, Natural Sprites and KITTI Masks, which we contribute as benchmarks for guiding disentanglement research towards more natural data domains.

1 Introduction

An intuitive approach to natural scene understanding is to decompose a scene into its underlying factors of variation [1]. This framing assumes that a visual representation of the world can be constructed via a generative process that receives factors of variation as input and produces natural signals as output. Although not true in the literal sense, this point of view is justified by the fact that our world is composed of distinct entities that can vary independently, but with regularity imposed by physics.

A long-standing goal in blind source separation and independent component analysis (ICA) [2–6] is to utilize such regularities to uncover the underlying factors of variation. Recently, unsupervised

*[†]Equal contribution. Code: https://github.com/bethgelab/slow_disentanglement

approaches towards this goal have largely been based on Variational Autoencoders (VAEs) [7] and have assumed that the data is independent and identically distributed (*i.i.d.*) [8]. Nonlinear methods that make this *i.i.d.* assumption have been proven to be *non-identifiable* [4], which means a set of possible solutions may all appear equally valid to the model, while only one identifies the true factors of variation. Previous attempts to avoid non-identifiability either require some form of supervision in practice [9–11], or are unsuited to model sparse transitions in natural scenes [9, 12, 13].

We contribute **SlowVAE**, a more parsimonious, unsupervised solution to nonlinear disentanglement. As opposed to requiring knowledge of the changing factors [9, 11] or having to infer the number of changes [10], we can prove our method’s identifiability using only the assumption of sparse transitions in natural scenes [14–16]. We further confirm this assumption with measurements from large-scale, natural, unstructured YouTube [17, 18] and KITTI [19–21] video annotations. We leverage this information to create novel datasets where the latent transitions between frames follow natural scene statistics, providing a benchmark to evaluate the practical capabilities of models in uncovering the true latent factors of variation in the presence of realistic dynamics. In summary:

- We present a set of video datasets that are increasingly more natural using measurements from natural scenes.
- We provide evidence that natural generative factors undergo sparse changes across time, which we exploit by extending the VAE framework with a sparse temporal prior.
- We provide theoretical justification for our model by proving that it is identifiable assuming temporal sparsity.
- We demonstrate improved disentanglement over previous models using quantitative metric evaluation across several datasets as well as visualizations of the learned manifolds.

2 Background

Disentangled representation learning [1] has its roots in blind source separation [2] and shares goals with many fields, such as inverse graphics [22, 23] and developing models of invariant neural computation [24, 25]. A disentangled representation would be valuable for a wide variety of machine learning applications, including sample efficiency for downstream tasks [8, 26], fairness [27, 28] and interpretability [1, 29, 30]. Since there is no agreed upon definition of disentanglement in the literature, we adopt two common measurable criteria: i) each encoding element represents a single generative factor and ii) the values of generative factors are trivially decodable from the encoding [31, 32]. ICA [33] provides an identifiable solution for disentangling data mixed via linear generators and non-Gaussian factors, but identifiability for nonlinear generators is impossible to achieve without additional constraints [4]. Nonetheless, the bottom-up approach of starting with a nonlinear generator that produces well-controlled data has led to considerable achievements in understanding nonlinear disentanglement in VAEs [29, 34–36], consolidating ideas from neural computation and machine learning [9], and seeking a principled definition of disentanglement [4, 32, 37, 38]. The motivation of our method and dataset contributions is to enable unsupervised disentanglement learning in more naturalistic scenarios.

Methods The fact that physical processes bind generative factors in temporally adjacent natural video segments has been thoroughly explored for learning in neural networks [14, 24, 39–41]. Recently, Hyvärinen and colleagues [12, 13, 42] showed that a solution to the non-identifiability of nonlinear ICA can be found by assuming that generative factors are conditioned on an additional observed variable, such as past states or the time index itself. This contribution was generalized by Khemakhem et al. [9] past the nonlinear ICA domain to any consistent parameter estimation method for deep latent-variable models, including the VAE framework. However, in their experiments they assume a semi-supervised setting by utilizing a label indicating the generating factor as their observed conditioning variable. Another branch of work considered learning disentangled representations from pairs of observations with uniform transition probabilities applied to a few factors of variation, while keeping the other factors fixed [10, 11, 43].

We propose a method that uses time information in the form of an L_1 -sparse temporal prior, which is motivated by the natural scene measurements presented below as well as by previous work [14–16, 44]. Such a prior would intuitively allow for sharp changes in some latent factors, while most other factors remain unchanged between adjacent time-points. Almost all similar methods are variants

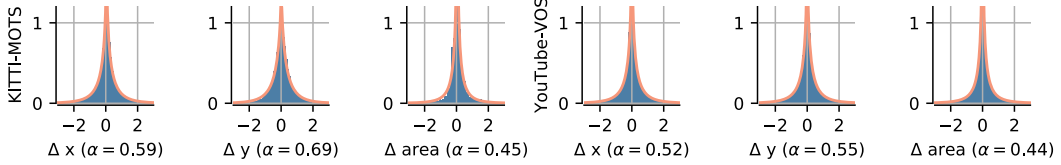


Figure 1: **Statistics of Natural Transitions.** Distribution over transitions for horizontal (Δx) and vertical (Δy) position as well as mask/object size (Δarea) for both datasets. Red lines indicate fits of generalized Laplace distributions (equation (2)) and α is the shape value estimate.

of slow feature analysis [24], which measure slowness in terms of the Euclidean (i.e. L_2 , or log Gaussian) distance between temporally adjacent encodings. An L_1 temporal prior has previously only been used in deep auto-encoder frameworks applied to semi-supervised tasks [45, 46], and was mentioned in [16], which used an L_2 prior, but claimed that an L_1 prior performed similarly on their task. Inspired by Hyvärinen et al. [12, 42], we only assume that the latent factors are temporally dependent, thus avoiding assuming knowledge of the number of factors where the two observations differ [11], which Locatello et al. [10] estimate during evaluation. We build on previous theory [9, 10] to provide a novel identifiability proof for our model under mild conditions. Reminiscent of linear ICA, we show analytically that identifiability up to a permutation hinges on non-Gaussian, sparse transitions across time. Together with our finding of highly leptokurtic transition distributions in natural data, we show that temporal sparse coding can serve as a parsimonious model for *unsupervised* nonlinear disentanglement².

Datasets The disentanglement library (DisLib) benchmark provided by Locatello et al. [8] has become an important model comparison resource by compiling datasets (dSprites [47], Cars3D [48], SmallNORB [49], Shapes3D [50], MPI3D [51]), metrics, and methods commonly used in the literature. All DisLib datasets are limited in that the data generating process is independent and identically distributed (*i.i.d.*) and all generative factors are assumed to be discrete. In the real world, however, almost all generative factors are continuous and exhibit structured temporal variation. In a follow-up study, Locatello et al. [10] proposed combining pairs of images such that only k factors change, where $k \in \mathcal{U}\{1, D - 1\}$ and D denotes the number of ground-truth factors (we refer to this data as LOC). We offer an alternative extension, contributing datasets augmented with natural continuous generative factors using measurements from large-scale, natural, unstructured videos. We evaluate using the metrics provided by DisLib and the Mean Correlation Coefficient, an additional metric common in the nonlinear ICA literature that allows for continuous variables (see Appendix B).

3 Natural Data

In order to construct our dataset and to inform our model prior, we extract segmentation masks from YouTube-VOS [17, 18] and KITTI-MOTS [19–21]. All analysis details are included in Appendix D. To inform our model prior, we compute statistics on measured transitions of area and position for object masks from YouTube-VOS and KITTI-MOTS. We visualize the distribution of transitions in Figure 1, where the red lines indicate generalized Laplacian (equation (2)) fits. A shape value of $\alpha = 0.5$ for these distributions corresponds to a kurtosis of 20. We see empirically that all distributions of temporal transitions are highly sparse.

From these measurements, we construct a progression of increasingly complex and more natural datasets (see summary below and details in Appendix C.3). Unlike the LOC data [10], for all of these datasets the object categories never change across transitions – reflecting natural object permanence. **Laplace Transitions (LAP)** is a procedure for constructing image pairs from DisLib datasets. For each ground-truth factor, the first value in the pair is chosen *i.i.d.* from the dataset and the second is chosen by weighting nearby factor values using Laplace distributed probabilities. If all factors remain constant (no transition), then the sample is rejected because the pair would not result in any temporal learning signal. **Natural Sprites** consists of pairs of sprite images. For a given image pair, the position and scale of the sprite objects are set using measured values from adjacent time points for natural objects in YouTube-VOS. The sprite shapes are simple, like dSprites, and fixed for a

²Learning from videos without labels, such as in slow feature analysis, is usually considered *unsupervised*.

given pair. The sprite orientations are fixed for the pair and are sampled uniformly from the same distribution as was used for dSprites. We also consider a discretized version of the dataset to evaluate standard DisLib metrics (see Appendix C.3.3 for details). **KITTI Masks** is composed of pedestrian segmentation masks from an autonomous driving vision benchmark KITTI-MOTS [19–21], with natural shapes and continuous natural transitions.

4 Generative Model

In the previous section we saw that generative factors of natural videos have sparse temporal transitions. To mimic this process, we assume temporally adjacent input pairs $(\mathbf{x}_{t-1}, \mathbf{x}_t)$ coming from a nonlinear generator that maps factors to images $\mathbf{x} = g(\mathbf{z})$, where pairs of generative factors form a Markov chain:

$$p(\mathbf{z}_t, \mathbf{z}_{t-1}) = p(\mathbf{z}_t | \mathbf{z}_{t-1}) p(\mathbf{z}_{t-1}). \quad (1)$$

Assume the observed data $(\mathbf{x}_t, \mathbf{x}_{t-1})$ comes from the following generative process:

$$\begin{aligned} \mathbf{x} = g(\mathbf{z}), \quad p(\mathbf{z}_{t-1}) &= \prod_{i=1}^d p(z_{t-1,i}), \\ p(\mathbf{z}_t | \mathbf{z}_{t-1}) &= \prod_{i=1}^d \frac{\alpha \lambda}{2\Gamma(1/\alpha)} \exp -(\lambda |z_{t,i} - z_{t-1,i}|)^\alpha, \end{aligned} \quad (2)$$

where $p(\mathbf{z}_{t-1})$ is a factorized Gaussian prior $\mathcal{N}(\mathbf{0}, \mathbf{I})$ (as in [7]) and $p(\mathbf{z}_t | \mathbf{z}_{t-1})$ is a factorized generalized Laplace distribution [52, 53] with shape parameter α , which determines the shape and especially the kurtosis of the function³. Intuitively, smaller α implies larger kurtosis and sparser temporal transitions of the generative factors (special cases are Gaussian, $\alpha = 2$, and Laplacian, $\alpha = 1$). Critically, for our proof we assume $\alpha < 2$ to ensure that temporal transitions are sparse. Like Locatello et al. [10], we assume that noise is modeled indirectly as a latent variable and is manifested through the generator g .

The main difference to Khemakhem et al. [9] is the form of the conditional prior $p(\mathbf{z}_t | \mathbf{z}_{t-1})$. They assume that the conditional posterior is part of the exponential family, but this does not include Laplacian conditionals. It is important to note that even though the exponential family contains the Laplace distribution with fixed mean as its member, this does not allow [9] to model sparse transitions. Khemakhem et al. [9] assume that the natural parameters of the exponential family distribution are conditioned on \mathbf{z}_{t-1} , meaning that only the scale and not the mean of the Laplace prior for \mathbf{z}_t can be modulated by the previous time step, thus not allowing for sparse transition probabilities.

4.1 Slow Variational Autoencoder

We build upon the framework of VAEs because of their efficiency in estimating a variational approximation to the ground truth posterior of a deep latent variable model [7]. The standard VAE objective assumes *i.i.d.* data and a standard normal prior with diagonal covariance on the learned latent representations $\mathbf{z} \sim \mathcal{N}(\mathbf{0}, \mathbf{I})$. To extend this to sequences, we assume the same functional form for our model prior as in equation (1) and (2).

Importantly, the posterior of our model is independent across time steps. Specifically,

$$\begin{aligned} q(\mathbf{z}_t, \mathbf{z}_{t-1} | \mathbf{x}_t, \mathbf{x}_{t-1}) &= q(\mathbf{z}_t | \mathbf{x}_t) q(\mathbf{z}_{t-1} | \mathbf{x}_{t-1}) \\ q(\mathbf{z} | \mathbf{x}) &= \prod_{i=1}^d \frac{1}{\sigma_i(\mathbf{x})\sqrt{2\pi}} \exp \left(-\frac{1}{2} \frac{(z_i - \mu_i(\mathbf{x}))^2}{\sigma_i^2(\mathbf{x})} \right), \end{aligned} \quad (3)$$

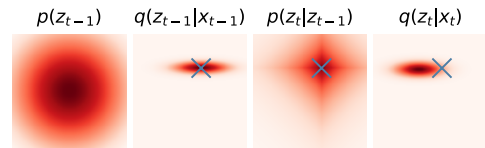


Figure 2: **SlowVAE illustration.** The prior and posterior for a two-dimensional latent space. Left to right: Normal prior for $t - 1$, posterior for $t - 1$, conditional Laplace prior for t , and posterior for t . The blue cross in the right three plots indicates the mean of the posterior for $t - 1$.

³For a stationary stochastic process, $p(\mathbf{z}_{t-1})$ represents the instantaneous marginal distribution and $p(\mathbf{z}_t | \mathbf{z}_{t-1})$ the transition distribution. In case of an autoregressive process with non-Gaussian innovations with finite variance, it follows from the central limit theorem that the marginal distribution converges to a Gaussian in the limit of large λ .

where $\mu_i(\mathbf{x})$ and $\sigma_i^2(\mathbf{x})$ are the input-dependent mean and variance of our model's posterior. We visualize this combination of priors and posteriors in Fig. 2.

The VAE learns a variational approximation to the true posterior by maximizing a lower bound on the log-likelihood of the empirical data distribution \mathcal{D}

$$E_{\mathbf{x}_{t-1}, \mathbf{x}_t \sim \mathcal{D}} [\log p(\mathbf{x}_{t-1}, \mathbf{x}_t)] \geq E_{\mathbf{x}_{t-1}, \mathbf{x}_t \sim \mathcal{D}} [E_{q(\mathbf{z}_t, \mathbf{z}_{t-1} | \mathbf{x}_t, \mathbf{x}_{t-1})} [\log p(\mathbf{x}_{t-1}, \mathbf{x}_t, \mathbf{z}_{t-1}, \mathbf{z}_t) - \log q(\mathbf{z}_t, \mathbf{z}_{t-1} | \mathbf{x}_t, \mathbf{x}_{t-1})]]. \quad (4)$$

For this, we need to compute the Kullback-Leibler divergence (KL) between the variational posterior and prior, which becomes (cf. Appendix A.2)

$$D_{KL}(q(\mathbf{z}_t, \mathbf{z}_{t-1} | \mathbf{x}_t, \mathbf{x}_{t-1}) | p(\mathbf{z}_t, \mathbf{z}_{t-1})) = D_{KL}(q(\mathbf{z}_{t-1} | \mathbf{x}_{t-1}) | p(\mathbf{z}_{t-1})) + E_{q(\mathbf{z}_{t-1} | \mathbf{x}_{t-1})} [D_{KL}(q(\mathbf{z}_t | \mathbf{x}_t) | p(\mathbf{z}_t | \mathbf{z}_{t-1}))]. \quad (5)$$

Thus, for a given pair of inputs $(\mathbf{x}_t, \mathbf{x}_{t-1})$, the full ELBO can be written as

$$\mathcal{L}(\mathbf{x}_t, \mathbf{x}_{t-1}) = E_{q(\mathbf{z}_t, \mathbf{z}_{t-1} | \mathbf{x}_t, \mathbf{x}_{t-1})} [\log p(\mathbf{x}_t, \mathbf{x}_{t-1} | \mathbf{z}_t, \mathbf{z}_{t-1})] - D_{KL}(q(\mathbf{z}_{t-1} | \mathbf{x}_{t-1}) | p(\mathbf{z}_{t-1})) - \gamma E_{q(\mathbf{z}_{t-1} | \mathbf{x}_{t-1})} [D_{KL}(q(\mathbf{z}_t | \mathbf{x}_t) | p(\mathbf{z}_t | \mathbf{z}_{t-1}))], \quad (6)$$

where γ is a regularization term for the sparsity prior, analogous to β in β -VAEs [29]. The first term on the right-hand side is the log-likelihood (i.e. the negative reconstruction error, with $p(\mathbf{x}_t, \mathbf{x}_{t-1} | \mathbf{z}_t, \mathbf{z}_{t-1})$ parameterized by the decoder of the VAE), the second term is the KL to a normal prior as in the standard VAE and the last term is an expectation of the KL between the posterior at time step t and the conditional prior $p(\mathbf{z}_t | \mathbf{z}_{t-1})$. The expectation in the last term is taken over samples from the posterior at the previous time step $q(\mathbf{z}_{t-1} | \mathbf{x}_{t-1})$. We observe that taking the mean $\mu(\mathbf{x}_{t-1})$ as a single sample is sufficient (analogous to the log-likelihood that is typically evaluated at a single sample from the posterior).

In practice, we need to choose α , λ , and γ . For the latter two, we can perform a random search for hyperparameters, as we discuss below. For the former, a parsimonious choice would be $\alpha = 1$, corresponding to a Laplace prior on the first temporal derivative of the latent code. For natural data, a value of $\alpha = 0.5$ would provide a better fit to Fig. 1, but a Laplace prior also achieves the goal of breaking the general rotation symmetry by having an optimum for axis-aligned representations, which is a requirement for identifiability. Therefore, we chose $\alpha = 1$ for this study. We derive a closed-form expression of the resulting KL in Appendix A.2.

4.2 Identifiability Result

Theorem 1 For a ground-truth $(g^*, \lambda^*, \alpha^*)$ and a learned (g, λ, α) model as defined in equation (2), if the functions g^* and g are injective and differentiable almost everywhere, $\lambda^* = \lambda$, $\alpha^* = \alpha < 2$ (i.e. there is no model misspecification) and the distributions of pairs of images generated from the priors $\mathbf{z}^* \sim p^*(\mathbf{z})$ and $\mathbf{z} \sim p(\mathbf{z})$ are matched $(g^*(\mathbf{z}_{t-1}^*), g^*(\mathbf{z}_t^*)) = (g(\mathbf{z}_{t-1}), g(\mathbf{z}_t))$ almost everywhere, then $g = g^* \circ \sigma$, where σ is a permutation with sign flipping.

The formal proof is provided in Appendix A.1. This result implies that if the temporal changes of ground-truth factors are sparse, then the only generator consistent with the observations is the ground-truth one (up to a permutation and sign flips). The main idea behind the proof is to represent g as $g^* \circ h$ and note that if h were not a permutation, then the distributions $((g^* \circ h)(\mathbf{z}_{t-1}), (g^* \circ h)(\mathbf{z}_t))$ and $(g^*(\mathbf{z}_{t-1}^*), g^*(\mathbf{z}_t^*))$ would not match, due to the injectivity of g^* .

Fig. 3 illustrates why the model defined in equation (2) has a unique generator. The crucial point is that we consider pairs of images, which differ effectively in only a few factors of variation due

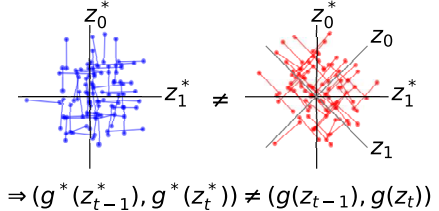


Figure 3: **Proof illustration.** Connected points indicate pairs of samples for the generative model (left) and for an entangled learned model (right). The relation means inequality in distribution.

| Model (Data) | BetaVAE | FactorVAE | MIG | DCI | Modularity | SAP |
|--------------------------------|-------------|-------------|------------|------------|------------|-----------|
| β -VAE (<i>i.i.d.</i>) | 82.3 | 66.0 | 10.2 | 18.6 | 82.2 | 4.9 |
| Ada-ML-VAE (LOC) | 89.6 | 70.1 | 11.5 | 29.4 | 89.7 | 3.6 |
| Ada-GVAE (LOC) | 92.3 | 84.7 | 26.6 | 47.9 | 91.3 | 7.4 |
| SlowVAE (LOC) | 90.4 (3.3) | 81.35 (7.6) | 35.7 (8.3) | 52.1 (6.5) | 87.6 (2.0) | 5.1 (1.4) |
| SlowVAE (LAP) | 100.0 (0.0) | 98.32 (2.5) | 27.8 (7.9) | 65.3 (3.1) | 97.0 (1.5) | 6.1 (2.6) |

Table 1: **DSprites**. Median and absolute deviation (a.d.) metric scores across 10 random seeds (first three rows are from [10]). Results for additional datasets and metrics are in Appendix D.

to the sparse prior ($\alpha < 2$). The 2D latent representations of such pairs are shown as blue points connected by lines. If the function h were not a permutation, it would map these latent points into a configuration in which many of the connecting lines are not parallel to one of the axes. However, the ground-truth generator, g^* , should still map this transformed latent space to the observed pairs of images differing in a few factors of variation, which contradicts it being injective. Moreover, Fig. 3 also illustrates that a rotationally symmetric Gaussian prior ($\alpha = 2$) on the transitions in either the generative or the learned model would make the problem non-identifiable. Similar to linear ICA, but in the temporal domain, we therefore have to assume that the transitions of generative factors across time be non-Gaussian.

5 Experiments

We evaluate models using the DisLib implementation for the following supervised metrics: BetaVAE [29]; FactorVAE [50]; Mutual Information Gap (MIG, [36]); Disentanglement, Compactness, and Informativeness (DCI [Disentanglement], [32]); Modularity [31]; and Separated Attribute Predictability (SAP, [54]) (see Appendix B for additional details). None of the DisLib metrics support ground-truth labels with continuous variation, which is required for evaluation on the continuous Natural Sprites and KITTI Masks datasets. To reconcile this, we measure the Mean Correlation Coefficient (MCC), a standard metric in the ICA literature [12] that is applicable to continuous variables. We report mean and standard deviation across 10 random seeds and bold-face significant (independent T-test, $p < 0.05$) improvements between models in all tables, except Tables 1 and 2 where we need to compare to the median values reported in [10].

To find the best hyperparameters for the conditional prior regularization and the prior rate, we perform a random search over $\gamma \in [1, 16]$ and $\lambda \in [1, 10]$ and compute the recently proposed unsupervised disentanglement ranking (UDR) scores for unsupervised model selection [55]. We notice that the optimal values are close to $\gamma = 10$ and $\lambda = 6$ on most datasets, so we use these values for all experiments. We leave it open to future work to find optimal values for specific datasets (which a practitioner can do with UDR), but note that it is a strong benefit of our approach that it works well with the same parameters across 13 datasets (counting different versions such as LAP and LOC), addressing a concern posed in [8]. Additional details on model selection and training can be found in Appendix C.2. For all visualizations, we pick the models with the highest disentanglement scores (see Appendix D).

5.1 Results on DisLib Benchmarks

We show the performance of all models on all metrics on the canonical benchmark dataset dSprites [47] in Table 1. The conclusions of our analyses generalize to the other datasets, which we report in Appendix D.

The models are trained on datasets which differ in the structure of their temporal transitions: β -VAE

| Model (Data) | SN | Cars3D | Shapes3D | MPI3D |
|--------------------------------|------------|------------|------------|------------|
| β -VAE (<i>i.i.d.</i>) | 21.4 | 8.8 | 22.0 | 7.2 |
| Ada-ML-VAE (LOC) | 31.1 | 14.7 | 50.9 | 24.1 |
| Ada-GVAE (LOC) | 25.6 | 15.0 | 56.2 | 28.4 |
| SlowVAE (LOC) | 23.2 (1.9) | 15.5 (1.4) | 66.4 (5.9) | 33.1 (1.2) |
| SlowVAE (LAP) | 25.4 (0.6) | 9.8 (1.4) | 62.9 (3.4) | 29.6 (1.1) |

Table 2: **DisLib Benchmarks**. Median (a.d.) MIG scores across 10 random seeds (first three rows are from [10]). SN refers to SmallNORB.

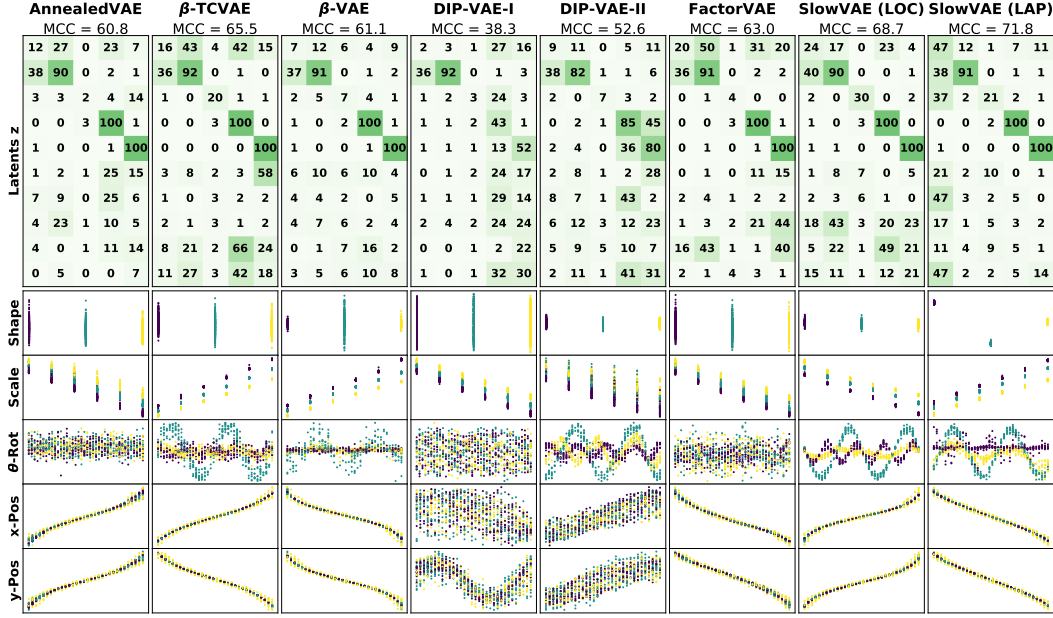


Figure 4: **DSprites Latent Representations:** (Top) shows absolute MCC between generative and model factors (rows are rearranged for maximal correlation on the main diagonal). The columns correspond to (shape, scale, rotation, x/y-position) and the values correspond to percent correlation. A more diagonal structure in the upper half corresponds to a better one-to-one mapping between generative and latent factors. (Bottom) shows individual latent dimensions (y-axis) over the matched generative factors (x-axis). Colors encode shapes: heart/yellow, ellipse/turquoise and square/purple.

is trained on non-temporal *i.i.d.* images; the models from [10] (Ada-ML-VAE and Ada-GVAE) are trained on image pairs where only k factors differ, as described in section 2 (LOC); and we show performance for SlowVAE trained on LOC as well as image pairs with sparse transitions that match the assumed prior (LAP). We do not evaluate MCC on the models of [10], as they are not released. We observe that SlowVAE models outperform the unsupervised baselines as well as the previous state of the art in nearly all metrics.

In Table 2, we report MIG scores across all datasets. In summary, we observe that SlowVAE trained on LOC outperforms the previous state of the art [10] in four out of the five benchmark datasets, with large gains especially on dSprites, Shapes3D and MPI3D. We note that the two datasets where we see the smallest performance differences (SmallNORB, Cars3D) have significantly more discrete categories (50, 183) than the other datasets (3 – 6). We suspect that the discrepancy can be attributed to these categorical variables, which do not have topological structure and might require different modeling approaches in future work.

Next, we visually compare the encodings for all model types compiled in DisLib. In our quantitative evaluation, we chose β -VAE as a representative model because the others perform similarly with regards to the quantitative metrics [8]. However, in Fig. 4 we observe that the different modeling assumptions result in differences in representation quality. To construct the visuals, we first compute the sorted correlation coefficient matrix between the latents and generative factors, which we visualize in the top row. The correlation matrix is sorted via linear sum assignment such that each ground-truth factor is associated with the latent variable with highest correlation. Each row of scatter plots corresponds to an individual generative factor. In each subplot, the horizontal axis indicates the ground truth value, the vertical axis indicates the corresponding latent value, and the colors indicate object shape. These plots aid in understanding how each ground-truth factor is encoded in the latent space in a way that is more informative than exclusively visualizing latent traversals or embeddings of pairs of latent units [43, 56–58]. For example, in the third row, we observe that SlowVAE trained on LOC shows three sinusoidal oscillations with equal phase, but frequencies $\sim \omega$, 2ω , and 4ω , which correspond to the three distinct rotational symmetries of the shapes: heart, ellipse and square.

| Model (Data) | BetaVAE | FactorVAE | MIG | DCI | Modularity | SAP | MCC |
|--------------|-------------------|-------------------|-------------------|-------------------|------------|------------------|-------------------|
| β -VAE | 78.1 (3.0) | 60.6 (6.0) | 4.6 (1.9) | 10.3 (1.8) | 87.8 (2.3) | 2.1 (1.0) | 41.7 (3.4) |
| SlowVAE | 82.6 (2.2) | 76.2 (4.8) | 11.7 (5.0) | 18.9 (5.5) | 88.1 (3.6) | 4.4 (2.3) | 52.6 (4.1) |

Table 3: **Discrete Natural Sprites.** Mean (s.d.) performance levels over 10 random seeds. Best models with statistical significance ($p < 0.05$) are indicated in bold.

| Model (Data) | MCC |
|------------------|-------------------|
| β -VAE (C) | 42.6 (4.7) |
| SlowVAE (C) | 49.1 (4.0) |

Table 4: **Continuous Natural Sprites.** Mean (s.d.) over 10 random seeds.

| Model (frame separation) | MCC |
|--------------------------|-------------------|
| β -VAE | 62.7 (7.1) |
| SlowVAE ($\Delta t=1$) | 66.1 (4.5) |
| SlowVAE ($\Delta t=5$) | 79.6 (5.8) |

Table 5: **KITTI Masks.** Mean (s.d.) over 10 random seeds.

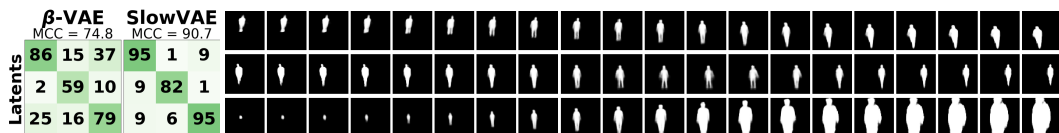


Figure 5: **KITTI Masks.** (Left) MCC correlation matrix of the top 3 latents corresponding to y-position, x-position and scale. (Right) Images produced by varying the SlowVAE ($\Delta t = 5$) latent unit that corresponds to the corresponding row in the MCC matrix.

5.2 Results on Natural Datasets

For discrete natural sprites, we observe that SlowVAE performs significantly better than β -VAE ($\beta = 8$, selected via UDR) on all metrics (Table 3). For continuous natural sprites, we observe again that SlowVAE outperforms β -VAE (Table 4). On the KITTI Masks dataset, one source of variation in the data source is the parameter that determines the temporal distance between sampled frames (Table 5). We run two settings ($\Delta t = 1, \Delta t = 5$) and observe that the benefit of temporal information is more apparent at $\Delta t = 5$. This links to recent work by Tschannen et al. [59], who show that temporal separation between frame embeddings influences the representation that is learned from videos. In Fig. 5, we can see that the SlowVAE has learned latent dimensions which have correspondence with the estimated ground truth factors of x/y-position and scale.

5.3 Towards an Approximate Theory of Disentanglement

In practice, a number of our theoretical assumptions are violated: After non-convex optimization, on a finite data sample, the distributions $p(\mathbf{x}_t, \mathbf{x}_{t-1})$ and $p^*(\mathbf{x}_t, \mathbf{x}_{t-1})$ are probably not perfectly matched. In addition, the model assumptions on $p(\mathbf{z}_t, \mathbf{z}_{t-1})$ likely do not fully match the distribution of the ground truth factors. For example, the model may be misspecified such that $\alpha \neq \alpha^*$ or $\lambda \neq \lambda^*$, or the chosen family of distributions may be incorrect altogether. In case of the DisLib data, the marginal distributions $p(\mathbf{z}_{t-1})$ are drawn from a Uniform (not Normal) distribution, and some of them are over unordered sets (categories) or bounded periodic spaces (rotation). Also, in practice the model latent space is usually chosen to have more dimensions than the ground truth generative model. On real data, factors of variation may be dependent [c.f. 60, 61]. Furthermore, the hypothesis class \mathcal{G} of learnable functions in the VAE architecture may not contain the invertible ground truth generator $g^* \notin \mathcal{G}$.

From ICA, it is common to assume that the distinction between subgaussian and supergaussian distributions is crucial, while detailed matching of the marginal distribution is generally less important [62]. In our current theory of nonlinear ICA such mismatch violates the assumptions needed for identifiability. However, in our experiments we see that approximate identification as measured by the different disentanglement metrics increases despite violations of theoretical assumptions, which is in line with prior studies [9–11]. Nevertheless, in future work, we would like to gain a better understanding of the theoretical and empirical consequences of such model misspecifications to move towards an approximate theory of disentanglement.

6 Conclusion

With the SlowVAE model we provide a parsimonious solution to identifiable nonlinear ICA that is inspired by a long history of learning visual representations from temporal data [39, 40]. We apply this model to the current metric-based disentanglement benchmarks and it outperforms existing approaches [10] across almost all metrics and datasets without any tuning of its hyperparameters to individual datasets. Additionally, we provide a benchmark of novel video datasets to guide disentanglement research towards more natural domains. Going beyond KITTI Masks, which is constrained, YouTube-VOS is a large-scale, unstructured, natural dataset with a sufficient number of samples to alleviate overfitting concerns. The Natural Sprites dataset serves as a tractable bridge to facilitate progress on the way to the more challenging YouTube-VOS. Taken together, our dataset and model proposals set the stage for utilizing knowledge of natural scene statistics to advance unsupervised disentangled representation learning.

Broader Impact

Representation learning is at the heart of model building for cognition. Our specific contribution is focused on core methods for modeling natural videos and the datasets used are more simplistic than real-world examples. However, foundational research on unsupervised representation learning has potentially large impact on AI for advancing the power of self-learning systems.

The broader field of representation learning has a large number of focused research directions that span machine learning and computational neuroscience. As such, the application space for this work is vast. For example, applications in unsupervised analysis of complicated and unintuitive data, such as medical imaging and gene expression information, have great potential to solve fundamental problems in health sciences. A future iteration of our disentangling approach could be used to encode such complicated data into a lower-dimensional and more understandable space that might reveal important factors of variation to medical researchers. Another important and complex modeling space that could potentially be improved by this line of research is in environmental sciences and combating global climate change.

Nonetheless, we acknowledge that any machine learning method can be used for nefarious purposes, which can be mitigated via effective, scientifically informed communication, outreach, and policy direction. We unconditionally denounce the use of derivatives of our work for weaponized or wartime applications. Additionally, due to the lack of interpretability generally found in modern deep learning approaches, it is possible for practitioners to inadvertently introduce harmful biases or errors in machine learning applications. Although we certainly do not solve this problem, our focus on providing identifiable solutions to representation learning is likely beneficial for both interpretability and fairness in machine learning.

Acknowledgments and Disclosure of Funding

The authors would like to thank Francesco Locatello for valuable discussions and providing numerical results to facilitate our experimental comparisons. Additionally, we thank Matthias Tangemann, Roland Zimmermann, Robert Geirhos, Matthias Kümmerer, Cornelius Schröder and Sarah Master for helpful feedback on the manuscript. Finally, the authors would like to thank Johannes Ballé, Jon Shlens and Eero Simoncelli for early discussions related to the ideas developed in this paper.

This work was supported by the Deutsche Forschungsgemeinschaft (DFG) in the priority program 1835 under grant BR2321/5-2 and by SFB 1233, Robust Vision: Inference Principles and Neural Mechanisms (TP3), project number: 276693517. We thank the International Max Planck Research School for Intelligent Systems (IMPRS-IS) for supporting LS and YS. DP was supported by the German Federal Ministry of Education and Research (BMBF) through the Tübingen AI Center (FKZ: 01IS18039A). IU, WB, and MB are supported by the Intelligence Advanced Research Projects Activity (IARPA) via Department of Interior/Interior Business Center (DoI/IBC) contract number D16PC00003. The U.S. Government is authorized to reproduce and distribute reprints for Governmental purposes notwithstanding any copyright annotation thereon. Disclaimer: The views and conclusions contained herein are those of the authors and should not be interpreted as necessarily representing the official policies or endorsements, either expressed or implied, of IARPA, DoI/IBC, or the U.S. Government.

The authors declare no conflicts of interests.

References

- [1] Yoshua Bengio, Aaron Courville, and Pascal Vincent. Representation learning: A review and new perspectives. *IEEE transactions on pattern analysis and machine intelligence*, 35(8):1798–1828, 2013.
- [2] Christian Jutten and Jeanny Herault. Blind separation of sources, part i: An adaptive algorithm based on neuromimetic architecture. *Signal Processing*, 24(1):1–10, 1991.
- [3] Anthony J Bell and Terrence J Sejnowski. An information-maximization approach to blind separation and blind deconvolution. *Neural Computation*, 7(6):1129–1159, 1995.
- [4] Aapo Hyvärinen and Petteri Pajunen. Nonlinear independent component analysis: Existence and uniqueness results. *Neural Networks*, 12(3):429–439, 1999.
- [5] Jonathan T Barron and Jitendra Malik. Shape, albedo, and illumination from a single image of an unknown object. In *2012 IEEE Conference on Computer Vision and Pattern Recognition*, pages 334–341. IEEE, 2012.
- [6] Jascha Sohl-Dickstein, Ching Ming Wang, and Bruno A Olshausen. An unsupervised algorithm for learning lie group transformations. *arXiv preprint arXiv:1001.1027*, 2010.
- [7] Diederik P Kingma and Max Welling. Auto-encoding variational bayes. *arXiv preprint arXiv:1312.6114*, 2013.
- [8] Francesco Locatello, Stefan Bauer, Mario Lucic, Gunnar Rätsch, Sylvain Gelly, Bernhard Schölkopf, and Olivier Bachem. Challenging common assumptions in the unsupervised learning of disentangled representations. *arXiv preprint arXiv:1811.12359*, 2018.
- [9] Ilyes Khemakhem, Diederik P Kingma, and Aapo Hyvärinen. Variational autoencoders and nonlinear ica: A unifying framework. *International Conference on Artificial Intelligence and Statistics (AISTATS)*, 2020.
- [10] Francesco Locatello, Ben Poole, Gunnar Rätsch, Bernhard Schölkopf, Olivier Bachem, and Michael Tschannen. Weakly-supervised disentanglement without compromises. *arXiv preprint arXiv:2002.02886*, 2020.
- [11] Rui Shu, Yining Chen, Abhishek Kumar, Stefano Ermon, and Ben Poole. Weakly supervised disentanglement with guarantees. *arXiv preprint arXiv:1910.09772*, 2019.
- [12] Aapo Hyvärinen and Hiroshi Morioka. Unsupervised feature extraction by time-contrastive learning and nonlinear ica. In *Advances in Neural Information Processing Systems*, pages 3765–3773, 2016.
- [13] Aapo Hyvärinen and Hiroshi Morioka. Nonlinear ica of temporally dependent stationary sources. In *Proceedings of Machine Learning Research*, 2017.
- [14] Aapo Hyvärinen, Jarmo Hurri, and Jaakko Väyrynen. Bubbles: a unifying framework for low-level statistical properties of natural image sequences. *JOSA A*, 20(7):1237–1252, 2003.
- [15] Bruno A Olshausen. Learning sparse, overcomplete representations of time-varying natural images. In *Proceedings 2003 International Conference on Image Processing (Cat. No. 03CH37429)*, volume 1, pages 1–41. IEEE, 2003.
- [16] Charles F Cadieu and Bruno A Olshausen. Learning intermediate-level representations of form and motion from natural movies. *Neural Computation*, 24(4):827–866, 2012.
- [17] Ning Xu, Linjie Yang, Yuchen Fan, Dingcheng Yue, Yuchen Liang, Jianchao Yang, and Thomas Huang. Youtube-vos: A large-scale video object segmentation benchmark. *arXiv preprint arXiv:1809.03327*, 2018.
- [18] Linjie Yang, Yuchen Fan, and Ning Xu. Video instance segmentation. *arXiv preprint arXiv:1905.04804*, 2019.
- [19] Paul Voigtlaender, Michael Krause, Aljosa Osep, Jonathon Luiten, Berin Balachandar Gnana Sekar, Andreas Geiger, and Bastian Leibe. Mots: Multi-object tracking and segmentation. *Conference on Computer Vision and Pattern Recognition (CVPR)*, 2019.
- [20] Andreas Geiger, Philip Lenz, and Raquel Urtasun. Are we ready for autonomous driving? the kitti vision benchmark suite. In *Conference on Computer Vision and Pattern Recognition (CVPR)*, 2012.
- [21] Anton Milan, Laura Leal-Taixé, Ian Reid, Stefan Roth, and Konrad Schindler. MOT16: A benchmark for multi-object tracking. *arXiv:1603.00831 [cs]*, March 2016.
- [22] Tejas D Kulkarni, William F Whitney, Pushmeet Kohli, and Josh Tenenbaum. Deep convolutional inverse graphics network. In *Advances in neural information processing systems*, pages 2539–2547, 2015.
- [23] Ilker Yildirim, Mario Belledonne, Winrich Freiwald, and Josh Tenenbaum. Efficient inverse graphics in biological face processing. *Science Advances*, 6(10):eaax5979, 2020.
- [24] Laurenz Wiskott and Terrence J Sejnowski. Slow feature analysis: Unsupervised learning of invariances. *Neural Computation*, 14(4):715–770, 2002.

[25] Aapo Hyvärinen and Patrik Hoyer. Emergence of phase-and shift-invariant features by decomposition of natural images into independent feature subspaces. *Neural computation*, 12(7):1705–1720, 2000.

[26] Lijian Gao, Qirong Mao, Ming Dong, Yu Jing, and Ratna Chinnam. On learning disentangled representation for acoustic event detection. In *Proceedings of the 27th ACM International Conference on Multimedia*, pages 2006–2014, 2019.

[27] Francesco Locatello, Gabriele Abbati, Thomas Rainforth, Stefan Bauer, Bernhard Schölkopf, and Olivier Bachem. On the fairness of disentangled representations. In *Advances in Neural Information Processing Systems*, pages 14611–14624, 2019.

[28] Elliot Creager, David Madras, Jörn-Henrik Jacobsen, Marissa A Weis, Kevin Swersky, Tonianne Pitassi, and Richard Zemel. Flexibly fair representation learning by disentanglement. In *International Conference on Machine Learning*, page 1436–1445, 2019.

[29] Irina Higgins, Loic Matthey, Arka Pal, Christopher Burgess, Xavier Glorot, Matthew Botvinick, Shakir Mohamed, and Alexander Lerchner. beta-vae: Learning basic visual concepts with a constrained variational framework. *International Conference on Learning Representations (ICLR)*, 2(5):6, 2017.

[30] Tameem Adel, Zoubin Ghahramani, and Adrian Weller. Discovering interpretable representations for both deep generative and discriminative models. In *International Conference on Machine Learning*, pages 50–59, 2018.

[31] Karl Ridgeway and Michael C Mozer. Learning deep disentangled embeddings with the f-statistic loss. In *Advances in Neural Information Processing Systems*, pages 185–194, 2018.

[32] Cian Eastwood and Christopher KI Williams. A framework for the quantitative evaluation of disentangled representations. In *In International Conference on Learning Representations*, 2018.

[33] Pierre Comon. Independent component analysis, a new concept? *Signal processing*, 36(3):287–314, 1994.

[34] Christopher P Burgess, Irina Higgins, Arka Pal, Loic Matthey, Nick Watters, Guillaume Desjardins, and Alexander Lerchner. Understanding disentangling in beta-vae. *arXiv preprint arXiv:1804.03599*, 2018.

[35] Michal Rolínek, Dominik Zietlow, and Georg Martius. Variational autoencoders pursue pca directions (by accident). In *Proceedings of the IEEE Conference on Computer Vision and Pattern Recognition*, pages 12406–12415, 2019.

[36] Tian Qi Chen, Xuechen Li, Roger B Grosse, and David K Duvenaud. Isolating sources of disentanglement in variational autoencoders. In *Advances in Neural Information Processing Systems*, pages 2610–2620, 2018.

[37] Irina Higgins, David Amos, David Pfau, Sébastien Racanière, Loic Matthey, Danilo Rezende, and Alexander Lerchner. Towards a definition of disentangled representations. *arXiv preprint arXiv:1812.02230*, 2018.

[38] Karl Ridgeway. A survey of inductive biases for factorial representation-learning. *arXiv preprint arXiv:1612.05299*, 2016.

[39] Geoffrey E Hinton. Connectionist learning procedures. In *Machine learning*, page 208. Elsevier, 1990.

[40] Peter Földiák. Learning invariance from transformation sequences. *Neural Computation*, 3(2):194–200, 1991.

[41] Graeme Mitchison. Removing time variation with the anti-hebbian differential synapse. *Neural Computation*, 3(3):312–320, 1991.

[42] Aapo Hyvärinen, Hiroaki Sasaki, and Richard E Turner. Nonlinear ica using auxiliary variables and generalized contrastive learning. *arXiv preprint arXiv:1805.08651*, 2018.

[43] Attila Szabó, Qiyang Hu, Tiziano Portenier, Matthias Zwicker, and Paolo Favaro. Challenges in disentangling independent factors of variation. *arXiv preprint arXiv:1711.02245*, 2017.

[44] Eero P Simoncelli and Bruno A Olshausen. Natural image statistics and neural representation. *Annual review of neuroscience*, 24(1):1193–1216, 2001.

[45] Hossein Mobahi, Ronan Collobert, and Jason Weston. Deep learning from temporal coherence in video. In *Proceedings of the 26th Annual International Conference on Machine Learning*, pages 737–744, 2009.

[46] Will Zou, Shenghuo Zhu, Kai Yu, and Andrew Y Ng. Deep learning of invariant features via simulated fixations in video. In *Advances in neural information processing systems*, pages 3203–3211, 2012.

[47] Loic Matthey, Irina Higgins, Demis Hassabis, and Alexander Lerchner. dsprites: Disentanglement testing sprites dataset. <https://github.com/deepmind/dsprites-dataset/>, 2017.

[48] Scott E Reed, Yi Zhang, Yuting Zhang, and Honglak Lee. Deep visual analogy-making. In *Advances in neural information processing systems*, pages 1252–1260, 2015.

[49] Yann LeCun, Fu Jie Huang, and Leon Bottou. Learning methods for generic object recognition with invariance to pose and lighting. In *Proceedings of the 2004 IEEE Computer Society Conference on Computer Vision and Pattern Recognition, 2004. CVPR 2004.*, volume 2, pages II–104. IEEE, 2004.

[50] Hyunjik Kim and Andriy Mnih. Disentangling by factorising. *arXiv preprint arXiv:1802.05983*, 2018.

[51] Muhammad Waleed Gondal, Manuel Wuthrich, Djordje Miladinovic, Francesco Locatello, Martin Breidt, Valentin Volchkov, Joel Akpo, Olivier Bachem, Bernhard Schölkopf, and Stefan Bauer. On the transfer of inductive bias from simulation to the real world: a new disentanglement dataset. In *Advances in Neural Information Processing Systems*, pages 15714–15725, 2019.

[52] Matthias Bethge. Factorial coding of natural images: how effective are linear models in removing higher-order dependencies? *JOSA A*, 23(6):1253–1268, 2006.

[53] Fabian Sinz, Sebastian Gerwinn, and Matthias Bethge. Characterization of the p-generalized normal distribution. *Journal of Multivariate Analysis*, 100(5):817–820, 2009.

[54] Abhishek Kumar, Prasanna Sattigeri, and Avinash Balakrishnan. Variational inference of disentangled latent concepts from unlabeled observations. In *International Conference on Learning Representations*, 2018.

[55] Sunny Duan, Loic Matthey, Andre Saraiva, Nick Watters, Christopher Burgess, Alexander Lerchner, and Irina Higgins. Unsupervised model selection for variational disentangled representation learning. In *International Conference on Learning Representations (ICLR)*, 2020.

[56] Brian Cheung, Jesse A Livezey, Arjun K Bansal, and Bruno A Olshausen. Discovering hidden factors of variation in deep networks. *arXiv preprint arXiv:1412.6583*, 2014.

[57] Xi Chen, Yan Duan, Rein Houthooft, John Schulman, Ilya Sutskever, and Pieter Abbeel. Infogan: Interpretable representation learning by information maximizing generative adversarial nets. In *Advances in neural information processing systems*, pages 2172–2180, 2016.

[58] Liqian Ma, Qianru Sun, Stamatios Georgoulis, Luc Van Gool, Bernt Schiele, and Mario Fritz. Disentangled person image generation. In *Proceedings of the IEEE Conference on Computer Vision and Pattern Recognition*, pages 99–108, 2018.

[59] Michael Tschannen, Josip Djolonga, Marvin Ritter, Aravindh Mahendran, Neil Houlsby, Sylvain Gelly, and Mario Lucic. Self-supervised learning of video-induced visual invariances. *arXiv preprint arXiv:1912.02783*, 2019.

[60] Frederik Träuble, Elliot Creager, Niki Kilbertus, Anirudh Goyal, Francesco Locatello, Bernhard Schölkopf, and Stefan Bauer. Is independence all you need? on the generalization of representations learned from correlated data. *arXiv preprint arXiv:2006.07886*, 2020.

[61] Mengyue Yang, Furui Liu, Zhitang Chen, Xinwei Shen, Jianye Hao, and Jun Wang. Causalvae: Structured causal disentanglement in variational autoencoder. *arXiv preprint arXiv:2004.08697*, 2020.

[62] Aapo Hyvärinen and Erkki Oja. Independent component analysis: algorithms and applications. *Neural networks*, 13(4-5):411–430, 2000.

[63] Stanisław Mazur and Stanisław Ulam. Sur les transformations isométriques d’espaces vectoriels normés. *CR Acad. Sci. Paris*, 194(946-948):116, 1932.

[64] Christopher M Bishop. *Pattern recognition and machine learning*. Springer, 2006.

[65] Emile Mathieu, Tom Rainforth, N Siddharth, and Yee Whye Teh. Disentangling disentanglement in variational autoencoders. In *Proceedings of the 36th International Conference on Machine Learning*, pages 4402–4412, 2019.

[66] Hiroshi Morioka. Time-contrastive learning (tcl), 2018. URL <https://github.com/hirosm/TCL>.

[67] Richard H Byrd, Peihuang Lu, Jorge Nocedal, and Ciyou Zhu. A limited memory algorithm for bound constrained optimization. *SIAM Journal on scientific computing*, 16(5):1190–1208, 1995.

[68] F. Pedregosa, G. Varoquaux, A. Gramfort, V. Michel, B. Thirion, O. Grisel, M. Blondel, P. Prettenhofer, R. Weiss, V. Dubourg, J. Vanderplas, A. Passos, D. Cournapeau, M. Brucher, M. Perrot, and E. Duchesnay. Scikit-learn: Machine learning in Python. *Journal of Machine Learning Research*, 12:2825–2830, 2011.

[69] Adam Paszke, Sam Gross, Francisco Massa, Adam Lerer, James Bradbury, Gregory Chanan, Trevor Killeen, Zeming Lin, Natalia Gimelshein, Luca Antiga, et al. Pytorch: An imperative style, high-performance deep learning library. In *Advances in Neural Information Processing Systems*, pages 8024–8035, 2019.

[70] Nicholas Watters, Loic Matthey, Sebastian Borgeaud, Rishabh Kabra, and Alexander Lerchner. Spriteworld: A flexible, configurable reinforcement learning environment, 2019. URL <https://github.com/deepmind/spriteworld/>.

Appendix

A Formal Methods

| Ground-truth model | Learned model | Description |
|-------------------------------------|---------------------------------|-----------------------|
| g^* | g | Generator |
| α^* | α | Prior shape |
| λ^* | λ | Prior rate |
| $p^*(\mathbf{z})$ | $p(\mathbf{z})$ | Prior |
| $\mathbf{z}^* \sim p^*(\mathbf{z})$ | $\mathbf{z} \sim p(\mathbf{z})$ | Latent variables |
| $\mathbf{x}^* = g^*(\mathbf{z}^*)$ | $\mathbf{x} = g(\mathbf{z})$ | Generated images |
| | $q(\mathbf{z} \mathbf{x})$ | Variational posterior |

Table 6: Glossary of terms.

A.1 Proof of Identifiability

To study disentanglement, we assume that the generative factors $\mathbf{z} \in \mathbb{R}^D$ are mapped to images $\mathbf{x} \in \mathbb{R}^N$ (usually $D << N$) by a nonlinear ground-truth generator $g^* : \mathbf{z} \mapsto \mathbf{x}$. We consider a representation with a learned generator g *disentangled* if it inverts the ground-truth generator in the sense that the composition $\sigma = (g^*)^{-1} \circ g$ can be described by a simple permutation and sign flips.

Theorem 1 *For a ground-truth $(g^*, \lambda^*, \alpha^*)$ and a learned (g, λ, α) generative model as defined in equation (2), if the following assumptions are satisfied:*

- The generators g^* and g are defined everywhere in the latent space. Moreover, they are injective and differentiable almost everywhere,
- There is no model misspecification i.e. $\alpha = \alpha^*$ and $\lambda = \lambda^*$, so $\mathbf{z} \sim p(\mathbf{z}) = p^*(\mathbf{z})$,
- Pairs of images are generated as $(\mathbf{x}_{t-1}^*, \mathbf{x}_t^*) = (g^*(\mathbf{z}_{t-1}), g^*(\mathbf{z}_t))$ and $(\mathbf{x}_{t-1}, \mathbf{x}_t) = (g(\mathbf{z}_{t-1}), g(\mathbf{z}_t))$,
- The distributions of $(\mathbf{x}_{t-1}^*, \mathbf{x}_t^*)$ and $(\mathbf{x}_{t-1}, \mathbf{x}_t)$ are the same (i.e. the corresponding densities are equal almost everywhere): $p^*(\mathbf{x}_{t-1}, \mathbf{x}_t) = p(\mathbf{x}_{t-1}, \mathbf{x}_t)$,

then $g = g^* \circ \sigma$, where σ is a composition of a permutation and sign flips.

Proof. Since $\mathbf{x} = g(\mathbf{z})$ can be written as $\mathbf{x} = (g^* \circ (g^*)^{-1} \circ g)(\mathbf{z})$, we can assume that $g = g^* \circ h$ for some function h on the latent space.

We first show that the function h is a bijection on the latent space. It is injective, since both g and g^* are injective. If it were not surjective, there would be a point $\tilde{\mathbf{z}}$ in the ground-truth latent space, which would not have a pre-image under h . Because of continuity of h , there would be some neighborhood $U_{\tilde{\mathbf{z}}}$ of $\tilde{\mathbf{z}}$ which would not have a pre-image under h . That would mean that images generated by g^* from $U_{\tilde{\mathbf{z}}}$ would have zero density under the distribution of images generated by g (i.e. $p(g^*(U_{\tilde{\mathbf{z}}})) = 0$), while this density would be non-zero under the distribution of images directly generated by the ground-truth generator g^* (i.e. $p^*(g^*(U_{\tilde{\mathbf{z}}})) \neq 0$), which contradicts the assumption that these distributions are equal. It follows that h is bijective.

In the next step, we show that the distribution of latent space pairs $(h(\mathbf{z}_{t-1}), h(\mathbf{z}_t))$ matches the latent space prior distribution (i.e. h preserves the prior distribution in the latent space). Indeed, using the assumption that the distributions of $(g^*(\mathbf{z}_{t-1}), g^*(\mathbf{z}_t))$ and $((g^* \circ h)(\mathbf{z}_{t-1}), (g^* \circ h)(\mathbf{z}_t))$ are the same, we can write the following equality using the change of variables formula:

$$\begin{aligned}
 p^*(\mathbf{x}_{t-1}, \mathbf{x}_t) &= p((g^*)^{-1}(\mathbf{x}_{t-1}), (g^*)^{-1}(\mathbf{x}_t)) \left| \det \left(\frac{d(g^*)^{-1}}{d(\mathbf{x}_{t-1}, \mathbf{x}_t)} \right) \right| \\
 &= p_h((g^*)^{-1}(\mathbf{x}_{t-1}), (g^*)^{-1}(\mathbf{x}_t)) \left| \det \left(\frac{d(g^*)^{-1}}{d(\mathbf{x}_{t-1}, \mathbf{x}_t)} \right) \right| = p(\mathbf{x}_{t-1}, \mathbf{x}_t),
 \end{aligned} \tag{7}$$

where p and p_h are densities of $(\mathbf{z}_{t-1}, \mathbf{z}_t)$ and $(h(\mathbf{z}_{t-1}), h(\mathbf{z}_t))$. Since the determinants above cancel, these densities are equal at the pre-image of any pair of images $(\mathbf{x}_{t-1}, \mathbf{x}_t)$. Because g^* is defined everywhere in the latent space, p and p_h are equal for any pair of latent space points. Applying the change of variables formula again, we obtain the following equation:

$$\begin{aligned} p(\mathbf{z}_{t-1}, \mathbf{z}_t) &= p(h^{-1}(\mathbf{z}_{t-1}), h^{-1}(\mathbf{z}_t)) \left| \det \left(\frac{dh^{-1}}{d(\mathbf{z}_{t-1}, \mathbf{z}_t)} \right) \right| \\ &= p(h^{-1}(\mathbf{z}_{t-1})) p(h^{-1}(\mathbf{z}_t) | h^{-1}(\mathbf{z}_{t-1})) \left| \det \left(\frac{dh^{-1}(\mathbf{z}_{t-1})}{d\mathbf{z}_{t-1}} \right) \right| \left| \det \left(\frac{dh^{-1}(\mathbf{z}_t)}{d\mathbf{z}_t} \right) \right| \quad (8) \\ &= p(\mathbf{z}_{t-1}) p(\mathbf{z}_t | \mathbf{z}_{t-1}). \end{aligned}$$

Note that the probability measure p is the same before and after the change of variables, since we showed that the prior distribution in the latent space must be invariant under the function h . The same condition for the marginal $p(\mathbf{z}_{t-1})$ is as follows:

$$p(\mathbf{z}_{t-1}) = p(h^{-1}(\mathbf{z}_{t-1})) \left| \det \left(\frac{dh^{-1}(\mathbf{z}_{t-1})}{d\mathbf{z}_{t-1}} \right) \right|. \quad (9)$$

Solving for the determinant of the Jacobian in (9) and plugging it into (8), we obtain

$$p(\mathbf{z}_t | \mathbf{z}_{t-1}) = p(h^{-1}(\mathbf{z}_t) | h^{-1}(\mathbf{z}_{t-1})) \frac{p(\mathbf{z}_t)}{p(h^{-1}(\mathbf{z}_t))}. \quad (10)$$

Taking logs of both sides, we arrive at the following equation:

$$A(\|\mathbf{z}_t - \mathbf{z}_{t-1}\|_\alpha^\alpha - \|h^{-1}(\mathbf{z}_t) - h^{-1}(\mathbf{z}_{t-1})\|_\alpha^\alpha) = B(\|\mathbf{z}_t\|_2^2 - \|h^{-1}(\mathbf{z}_t)\|_2^2), \quad (11)$$

where A and B are the constants appearing in the exponentials in $p(\mathbf{z}_{t-1})$ and $p(\mathbf{z}_t | \mathbf{z}_{t-1})$. The logs of normalization constants cancel out.

For any \mathbf{z}_t we can choose $\mathbf{z}_{t-1} = \mathbf{z}_t$ making the left hand side in (11) equal to zero. This implies that $\|\mathbf{z}_t\|_2^2 = \|h^{-1}(\mathbf{z}_t)\|_2^2$ for any \mathbf{z}_t , i.e. function h^{-1} preserves the 2-norm. Moreover, the preservation of the 2-norm implies that $p(\mathbf{z}_{t-1}) = p(h^{-1}(\mathbf{z}_{t-1}))$ and therefore it follows from (9) that for any \mathbf{z}

$$\left| \det \left(\frac{dh^{-1}(\mathbf{z})}{d\mathbf{z}} \right) \right| = 1. \quad (12)$$

Thus, the left hand side of (11) can be re-written as

$$\|\mathbf{z}_t - \mathbf{z}_{t-1}\|_\alpha^\alpha - \|h^{-1}(\mathbf{z}_t) - h^{-1}(\mathbf{z}_{t-1})\|_\alpha^\alpha = 0. \quad (13)$$

This means that h^{-1} preserves the α -distances between points. Moreover, because h is bijective, the Mazur-Ulam theorem [63] tells us that h must be an affine transform.

In the next step, to prove that h must be a permutation and sign flip, let us choose an arbitrary point \mathbf{z}_{t-1} and $\mathbf{z}_t = \mathbf{z}_{t-1} + \varepsilon \mathbf{e}_k = (z_{1,1}, \dots, z_{1,k} + \varepsilon, \dots, z_{1,D})$. Using (13) and performing a Taylor expansion around \mathbf{z}_{t-1} , we obtain the following:

$$\begin{aligned} \varepsilon^\alpha &= \|\mathbf{z}_t - \mathbf{z}_{t-1}\|_\alpha^\alpha \\ &= \|h^{-1}(\mathbf{z}_{t-1} + \varepsilon \mathbf{e}_k) - h^{-1}(\mathbf{z}_{t-1})\|_\alpha^\alpha \\ &= \left\| \varepsilon \cdot \left(\frac{\partial h_1^{-1}(\mathbf{z}_{t-1})}{\partial z_{t-1,k}}, \dots, \frac{\partial h_D^{-1}(\mathbf{z}_{t-1})}{\partial z_{t-1,k}} \right) + O(\varepsilon^2) \right\|_\alpha^\alpha. \end{aligned} \quad (14)$$

The higher-order terms $O(\varepsilon^2)$ are zero since h is affine, therefore dividing both sides of the above equation by ε^α we find that

$$\left\| \left(\frac{\partial h_1^{-1}(\mathbf{z}_{t-1})}{\partial z_{t-1,k}}, \dots, \frac{\partial h_D^{-1}(\mathbf{z}_{t-1})}{\partial z_{t-1,k}} \right) \right\|_\alpha^\alpha = 1. \quad (15)$$

The vectors of k -th partial derivatives of components of h^{-1} are columns of the Jacobian matrix $\left(\frac{dh^{-1}(\mathbf{z})}{d\mathbf{z}}\right)$. Using the fact that the determinant of that matrix is equal to one and applying Hadamard's inequality, we obtain that

$$\left| \det \left(\frac{dh^{-1}(\mathbf{z})}{d\mathbf{z}} \right) \right| = 1 \leq \prod_{k=1}^D \left\| \left(\frac{\partial h_1^{-1}(\mathbf{z}_{t-1})}{z_{t-1,k}}, \dots, \frac{\partial h_D^{-1}(\mathbf{z}_{t-1})}{z_{t-1,k}} \right) \right\|_2. \quad (16)$$

Since $\alpha < 2$, for any vector \mathbf{v} it holds that $\|\mathbf{v}\|_2 \leq \|\mathbf{v}\|_\alpha$, with equality only if at most one component of \mathbf{v} is non-zero. This inequality implies that both (15) and (16) hold at the same time if and only if

$$\left\| \left(\frac{\partial h_1^{-1}(\mathbf{z}_{t-1})}{z_{t-1,k}}, \dots, \frac{\partial h_D^{-1}(\mathbf{z}_{t-1})}{z_{t-1,k}} \right) \right\|_2 = \left\| \left(\frac{\partial h_1^{-1}(\mathbf{z}_{t-1})}{z_{t-1,k}}, \dots, \frac{\partial h_D^{-1}(\mathbf{z}_{t-1})}{z_{t-1,k}} \right) \right\|_\alpha = 1, \quad (17)$$

meaning that only one element of these vectors of k -th partial derivatives is non-zero, and it is equal to 1 or -1. Thus, the function h is a composition of a permutation and sign flips at every point. Potentially, this permutation might be input-dependent, but we argued above that h is affine, therefore the permutation must be the same for all points. \square

A.2 Kullback Leibler Divergence

As part of the model's learning objective equation (6) we need to compute the KL divergence between the posterior $q(\mathbf{z}_t, \mathbf{z}_{t-1} | \mathbf{x}_t, \mathbf{x}_{t-1})$ and the prior $p(\mathbf{z}_t, \mathbf{z}_{t-1})$. Since all of these distributions are per design factorial, we will, for simplicity, derive the KL below for scalar variables (log-probabilities will simply have to be summed to obtain the full expression). Recall that the model prior and posterior factorize like

$$\begin{aligned} p(z_t, z_{t-1}) &= p(z_t | z_{t-1}) p(z_{t-1}) \\ q(z_t, z_{t-1} | \mathbf{x}_t, \mathbf{x}_{t-1}) &= q(z_t | \mathbf{x}_t) q(z_{t-1} | \mathbf{x}_{t-1}). \end{aligned} \quad (18)$$

Then, given a pair of inputs $(\mathbf{x}_{t-1}, \mathbf{x}_t)$, the KL can be written

$$\begin{aligned} D_{KL}(q(z_t, z_{t-1} | \mathbf{x}_t, \mathbf{x}_{t-1}) | p(z_t, z_{t-1})) &= E_{z_t, z_{t-1} \sim q(z_t, z_{t-1} | \mathbf{x}_t, \mathbf{x}_{t-1})} \left[\log \frac{q(z_t | \mathbf{x}_t) q(z_{t-1} | \mathbf{x}_{t-1})}{p(z_t | z_{t-1}) p(z_{t-1})} \right] \\ &= E_{z_{t-1} \sim q(z_{t-1} | \mathbf{x}_{t-1})} \left[\log \frac{q(z_{t-1} | \mathbf{x}_{t-1})}{p(z_{t-1})} \right] + E_{z_t, z_{t-1} \sim q(z_t, z_{t-1} | \mathbf{x}_t, \mathbf{x}_{t-1})} \left[\log \frac{q(z_t | \mathbf{x}_t)}{p(z_t | z_{t-1})} \right] \\ &= D_{KL}(q(z_{t-1} | \mathbf{x}_{t-1}) | p(z_{t-1})) - H(q(z_t | \mathbf{x}_t)) + E_{z_{t-1} \sim q(z_{t-1} | \mathbf{x}_{t-1})} [H(q(z_t | \mathbf{x}_t), p(z_t | z_{t-1}))] \end{aligned} \quad (19)$$

Where we use the fact that KL divergences decompose like $D_{KL}(X, Y) = H(X, Y) - H(X)$ into (differential) cross-entropy $H(X, Y)$ and entropy $H(X)$. The first term of the last line in (19) is the same KL divergence as in the standard VAE, namely between a Gaussian distribution $q(z_{t-1} | \mathbf{x}_{t-1})$ with some $\mu(\mathbf{x}_{t-1})$ and $\sigma(\mathbf{x}_{t-1})$ and a standard Normal distribution $p(z_{t-1})$. The solution of the KL is given by $D_{KL}(q(z_{t-1} | \mathbf{x}_{t-1}) | q(z_{t-1})) = -\log \sigma(\mathbf{x}_{t-1}) + \frac{1}{2}(\mu(\mathbf{x}_{t-1})^2 + \sigma(\mathbf{x}_{t-1})^2 - 1)$ [64]. The second term on the RHS, i.e. the entropy of a Gaussian is simply given by $H(q(z_t | \mathbf{x}_t)) = \log(\sigma(\mathbf{x}_t) \sqrt{2\pi e})$.

To compute the last term on the RHS, let us recall the Laplace form of the conditional prior

$$p(z_t | z_{t-1}) = \frac{\lambda}{2} \exp -\lambda |z_t - z_{t-1}|. \quad (20)$$

Thus the cross-entropy becomes

$$\begin{aligned} H(q(z_t | \mathbf{x}_t), p(z_t | z_{t-1})) &= -E_{z_t \sim q(z_t | \mathbf{x}_t)} [\log p(z_t | z_{t-1})] \\ &= -\log \left(\frac{\lambda}{2} \right) + \lambda E_{z_t \sim q(z_t | \mathbf{x}_t)} [|z_t - z_{t-1}|]. \end{aligned} \quad (21)$$

Now, if some random variable $X \sim \mathcal{N}(\mu, \sigma^2)$, then $Y = |X|$ follows a *folded normal distribution*, for which the mean is defined as

$$E[|x|] = \sigma \sqrt{\frac{2}{\pi}} \exp\left(-\frac{\mu^2}{2\sigma^2}\right) - \mu \left(1 - 2\Phi\left(\frac{\mu}{\sigma}\right)\right), \quad (22)$$

where Φ is the cumulative distribution function of a standard normal distribution (mean zero and variance one). Thus, denoting $\mu(\mathbf{x}_t, z_{t-1}) = \mu(\mathbf{x}_t) - z_{t-1}$, we can rewrite further

$$\begin{aligned} & H(q(z_t | \mathbf{x}_t), p(z_t | z_{t-1})) = \\ & -\log\left(\frac{\lambda}{2}\right) + \lambda \left(\sigma(\mathbf{x}_t) \sqrt{\frac{2}{\pi}} \exp\left(-\frac{\mu(\mathbf{x}_t, z_{t-1})^2}{2\sigma(\mathbf{x}_t)^2}\right) - \mu(\mathbf{x}_t, z_{t-1}) \left(1 - 2\Phi\left(\frac{\mu(\mathbf{x}_t, z_{t-1})}{\sigma(\mathbf{x}_t)}\right)\right) \right). \end{aligned} \quad (23)$$

B Disentanglement Metrics

Several recent studies have brought to light shortcomings in a number of proposed disentanglement metrics [32, 36, 37, 50, 65], many of which have been compiled in the DisLib benchmark. In addition to the concerns they raise, it is important to note that none of the supervised metrics implemented in DisLib allow for continuous ground-truth factors, which is necessary for evaluating with the Natural Sprites and KITTI Masks datasets, as factors such as position and scale are effectively continuous in reality. To rectify this issue without introducing novel metrics, we include the Mean Correlation Coefficient (MCC) as implemented by Hyvärinen and Morioka [12], which is described below.

We measure all metrics presented below between 10,000 samples of latent factors \mathbf{z} and the corresponding encoded means of our model $\mu(g^*(\mathbf{z}))$. We increase this sample size to 100,000 for Modularity and MIG to stabilize the entropy estimates.

B.1 Mean Correlation Coefficient

In addition to the DisLib metrics, we also compute the Mean Correlation Coefficient (MCC) in order to perform quantitative evaluation with continuous variables. Because of Theorem 1, perfect disentanglement in the noiseless case should always lead to a correlation coefficient of 1 or -1 , although note that we report 100 times the absolute value of the correlation coefficient. In our experiments, MCC is used without modification from the authors' open-sourced code [66]. The method first measures correlation between the ground-truth factors and the encoded latent variables. The initial correlation matrix is then used to match each latent unit with a preferred ground-truth factor. This is an assignment problem that can be solved in polynomial time via the Munkres algorithm, as described in the code release [66]. After solving the assignment problem, the correlation coefficients are computed again for the vector of ground-truth factors and the resulting permuted vector of latent encodings, where the output is a matrix of correlation coefficients with D columns for each ground-truth factor and D' rows for each latent variable. We use the (absolute value of the) Spearman coefficient as our correlation measure which assumes a monotonic relationship between the ground-truth factors and latent encodings but tolerates deviations from a strictly linear correspondence.

In the existing implementation for MCC, the ground truth factors, latent encodings, and mixed signal inputs are assumed to have the same dimensionality, i.e. $D = D' = N$. However, in our case, the ground-truth generating factors are much lower dimensional than the signal, $N \ll D$, and the latent encoding is higher dimensional than the ground-truth factors $D' > D$ (see Appendix C.2 for details). To resolve this discrepancy, we add $D' - D$ standard Gaussian noise channels to the ground-truth factors. To compute the MCC score, we take the mean of the absolute value of the upper diagonal of the correlation matrix. The upper diagonal is the diagonal of the square matrix of D ground-truth factors by the top D most correlated latent dimensions after sorting. In this way, we obtain an MCC estimate which averages only over the D correlation coefficients of the D ground truth factors with their corresponding best matching latent factors,

B.2 DisLib Metrics

BetaVAE [29]

BetaVAE uses a biased estimator with tunable hyperparameters, although we follow the convention established in [8] of using the *scikit-learn* defaults. For a sample in a batch, a pair of images, $(\mathbf{x}_1, \mathbf{x}_2)$, is generated by fixing the value of one of the data generative factors while uniformly sampling the rest. The absolute value of the difference between the latent codes produced from the image pairs is then taken, $\mathbf{z}_{\text{diff}} = |\mathbf{z}_1 - \mathbf{z}_2|$. A logistic classifier is fit with batches of \mathbf{z}_{diff} variables and the corresponding index of the fixed ground-truth factor serves as the label. Once the classifier is trained, the metric itself is the mean classifier accuracy on a batch of held-out test data. The training minimizes the following loss:

$$L = \frac{1}{2} \mathbf{w}^T \mathbf{w} + \sum_{i=1}^n \log(\exp(-\mathbf{y}_i(\mathbf{z}_{\text{diff},i}^T \mathbf{w} + c)) + 1), \quad (24)$$

where \mathbf{w} and c are the learnable weight matrix and bias, respectively, and \mathbf{y} is the index of the fixed ground-truth factor for the batch. The network is trained using the `lbfgs` optimizer [67], which is implemented via the *scikit-learn* Python package [68] in `disentanglement_lib` [8]. In the original work, the authors argue that their metric improves over a correlation metric such as the mean correlation coefficient by additionally measuring interpretability, although the linear operation of $\mathbf{z}_{\text{diff},i}^T \mathbf{w} + c$ can perform demixing, which means the measure gives no direct indication of identifiability and thus does not guarantee that the latent encodings are interpretable, especially in the case of dependent factors. Additionally, as noted by Kim and Mnih [50], BetaVAE can report perfect accuracy when all but one of the ground-truth factors are disentangled, since the classifier can trivially attribute the remaining factor to the remaining latents.

FactorVAE [50]

For FactorVAE, the variance of the latent encodings is computed for a large (10,000 in DisLib) batch of data where all factors could possibly be changing. Latent dimensions with variance below some threshold (0.05 in DisLib) are rejected and not considered further. Next, the encoding variance is computed again on a smaller batch (64 in DisLib) of data where one factor is fixed during sampling. The quotient of these two quantities (with the larger batch variance as the denominator) is then taken to obtain a normalized variance estimate per latent factor. Finally, a majority-vote classifier is trained to predict the index of the ground-truth factor with the latent unit that has the lowest normalized variance. The FactorVAE score is the classification accuracy for a batch of held-out data.

Mutual Information Gap [36]

The Mutual Information Gap (MIG) metric was introduced as an alternative to the classifier-based metrics that we discuss herein. It provides a normalized measure of the mean difference in mutual information between each ground truth factor and the two latent codes that have the highest mutual information with the given ground truth factor. As it is implemented in DisLib, MIG measures entropy by discretizing the model’s latent code using a histogram with 20 bins equally spaced between the representation minimum and maximum. It then computes the discrete mutual information between the ground-truth values and the discretized latents using the `scikit-learn metrics.mutual_info_score` function [68]. For the normalization it divides this difference by the entropy of the discretized ground truth factors.

Modularity [31]

Ridgeway and Mozer [31] measure disentanglement in terms of three factors: modularity, compactness, and explicitness. For modularity, they first measure the mutual information between the discretized latents and ground-truth factors using the same histogram procedure that was used for the MIG, resulting in a matrix, $M \in \mathbb{R}^{D' \times D}$ with entries for each mutual information pair. Their measure of modularity is then

$$\text{modularity} = \frac{1}{D'} \sum_{i=1}^{D'} \Theta \left(1 - \frac{\sum_{j=1}^D M_{i,j}^2 - \max(M_i^2)}{\max(M_i^2)(D-1)} \right), \quad (25)$$

where $\max(M_i^2)$ returns the maximum of the vector of squared mutual information measurements between ground truth i and each latent factor. Additionally, Θ is a selection function that returns zero for any i where $\max(M_i^2) = 0$ and otherwise acts as the identity function.

DCI Disentanglement [32]

The DCI scores measure disentanglement, completeness, and informativeness, which have intuitive correspondence to the modularity, compactness, and explicitness of [31], respectively. To measure DCI Disentanglement, D regressors are trained to predict each ground truth factor state given the latent encoding. The DisLib implementation uses the `ensemble.GradientBoostingClassifier` function from *scikit-learn* with default parameters, which trains D gradient boosted logistic regression tree classifiers. Importance is assigned to each latent factor using the built-in `feature_importance_` property of the classifier, which computes the normalized total reduction of the classifier criterion loss contributed by each latent. Disentanglement is then measured as

$$\sum_{i=1}^D D(1 - H(I_i))\tilde{I}_i, \quad (26)$$

where H is the entropy computed with the `stats.entropy` function from *scikit-learn*, $I \in \mathbb{R}^{D \times D'}$ is a matrix of the absolute value of the feature importance between each factor and each ground truth, and \tilde{I} is a normalized version of the matrix

$$\tilde{I}_i = \frac{\sum_{j=1}^{D'} I_{i,j}}{\sum_{k=1}^D \sum_{j=1}^{D'} I_{k,j}} \quad (27)$$

SAP Score [54]

To compute the SAP score, Kumar et al. [54] first train a linear support vector classifier with squared hinge loss and L_2 penalty to predict each ground truth factor from each latent variable. In DisLib this is implemented with the `svm.LinearSVC` function with default parameters from *scikit-learn*. They construct a score matrix $S \in \mathbb{R}^{D' \times D}$, where each entry in the matrix is the batch-mean classifier accuracy for predicting each ground truth given each individual latent encoding. For each generative factor, they compute the difference between the top two most predictive latent dimensions, which are the two highest scores in a given column of S . The mean (across ground-truth factors) of these differences is the SAP score.

C Methods

C.1 Model training and selection

We train all models on all datasets provided in DisLib with the **LOC** and **LAP** variants. We also train SlowVAE and β -VAE on **Natural Sprites** and **KITTI Masks**. When available, we compare scores directly using models we train, otherwise we reprint scores reported in [10].

C.2 Implementation Details

All models are implemented in PyTorch [69]. To facilitate comparison, the training parameters, e.g. optimizer, batch size, number of training steps, as well as the VAE encoder and decoder architecture are identical to those reported in [8, 10]. We use this architecture for all datasets, only adjusting the number of input channels (greyscale for dSprites, smallNORB, and KITTI Masks; three color channels for all other datasets).

The model formulation is agnostic to the direction of time. Therefore, to increase the temporal training signal at a fixed computational cost for each batch of input pairs $(\mathbf{x}_0, \mathbf{x}_1)$, we optimize the model in both directions i.e. optimizing the model objective for both $t_0 = 0, t_1 = 1$ as well as $t_0 = 1, t_1 = 0$.

C.3 Natural Datasets

We introduce several datasets to investigate disentanglement in more natural scenarios. Here, we provide a detailed description on the design of each dataset.

C.3.1 Laplace transitions

For each of the datasets in DisLib, we collect pairs of images. For each ground-truth factor, the first value in the pair is chosen from a uniform distribution across all possible values in latent space,

while the second is chosen by weighting nearby values in latent space using Laplace distributed probabilities (see equation 2). Since we are restricted to the set of given factor values, the dataset has edge conditions where samples that would push a factor outside the preset range are rejected. This may, however, alleviate issues introduced by rotation symmetries since, under this Laplace prior in the latent space, it is extremely unlikely to observe ‘large’ transitions from orientations of $\theta = 2\pi - \epsilon$ to $\theta = \epsilon$. This dataset introduces a hyper-parameter λ that controls the rate of the Laplace sampling distribution, while the location is set by the initial factor value. Effectively, when this rate is $\lambda = 1$ most of the factors change most of the time, whereas for a rate of $\lambda = 10$ most of the factors will not change most of the time (recall that we reject samples without any changes, so at least one factor will change in every valid sample). To maximize comparability with [10], for each pair of inputs we sample the rate of the Laplace prior from a uniform distribution $\lambda \sim \mathcal{U}(1, 10)$. This correspond to the setting ($k = \text{rand}$) in the LOC data, which is reported throughout the paper.

C.3.2 YouTube-VOS

For the YouTube dataset, we download annotations from the 2019 version of the video instance segmentation (Youtube-VIS) dataset [18]⁴, which is built on top of the video object segmentation (Youtube-VOS) dataset [17]. The dataset has annotations for every five frames in a 30fps video, which results in a 6fps sampling rate. The authors believe that the temporal correlation between five consecutive frames is sufficiently strong that annotations can be omitted for intermediate frames to reduce the annotation efforts. Such a skip-frame annotation strategy enables scaling up the number of videos and objects annotated under the same budget, yielding 131,000 annotations for 2,883 videos, with 4,883 unique video object instances.

The original image size of the dataset is 720×1280 . In order to preserve the statistics of the transitions, we choose not to directly downsample to 64×64 , but instead preserve the aspect ratio by downsampling to 64×128 . In order to minimize the bias yielded by the extraction method, noting the center bias typically present in human videos, we extract three equally spaced 64×64 pixel windows (with overlap) with a stride of 32.

For each resulting $64 \times 64 \times T$ sequence, where T denotes the number of time steps in the sequence, we filter out all pairs where the given object instance is not present in adjacent frames, resulting in 234,652 pairs.

An issue with evaluating disentanglement on natural datasets is the fact that the existing disentanglement metrics require knowledge of the underlying generative process of the given data. Although we can observe that the world is composed of distinct entities that vary according to rules imposed by physics, we are unable to determine the precise “factors” that generate such scenes. To mitigate this problem, we compile object measurements by calculating the x and y coordinates of the center of mass as well as the area of each object in each frame. We use these measurements to a) augment existing disentanglement benchmarks with natural transitions (Natural Sprites) and b) evaluate the ability of algorithms to decode intrinsic object properties (KITTI Masks).

C.3.3 Natural Sprites

Without a definition of disentanglement that can be applied to unknown data generating processes, we are limited to synthetic datasets with known ground-truth factors. Let us take dSprites [47] as an example. The dataset consists of all combinations of a set of latent factor values, namely,

- Color: white
- Shape: square, ellipse, heart
- Scale: 6 values linearly spaced in $[0.5, 1]$
- Orientation: 40 values in $[0, 2\pi]$
- Position X : 32 values in $[0, 1]$
- Position Y : 32 values in $[0, 1]$

Given the limited set of discrete values each factor can take on, all possible samples can be described by a tractable dataset, compiled and released to the public. But, in reality, all of these factors should be

⁴<https://competitions.codalab.org/competitions/20127>

| Config | Scale | X | Y | (R, G, B) | Shape | Orientation |
|------------|-----------|-------------|-------------|-----------------|-------------------------------------|-------------------|
| Continuous | YT [2375] | YT [197342] | YT [187112] | (1.0, 1.0, 1.0) | (square, triangle, star_4, spoke_4) | (0.9,...,342,351) |
| Discrete | YT [6] | YT [32] | YT [32] | (1.0, 1.0, 1.0) | (square, triangle, star_4, spoke_4) | (0.9,...,342,351) |

Table 7: Natural Sprite Configs. Values in brackets refer to the number of unique values. Shapes presented are predefined in Spriteworld [70].

continuous: a spectrum of possible colors, shapes, scales, orientations, and positions exist. We address this by constructing a dataset that is augmented with natural and continuous ground truth factors, using the mask properties measured from the large-scale, natural, unstructured YouTube [17, 18] dataset.

We can choose the complexity of the dataset by discretizing the 234,652 transition pairs of position and scale into an arbitrary number of bins. In this study, we discretize to match dSprites, which we present in Table 7. We produce a pair by fixing the color, shape, and orientation, but updating the position and scale with transitions sampled from the YouTube measurements. To minimize the effect of extreme outliers, we filter out 10% of the data by removing frames if the mask area falls below the 5% or above the 95% quantiles, which reduces the number of pairs to 207,794. Finally, we use the Spriteworld [70] renderer to generate the images. The benchmark is available at <https://zenodo.org/record/3948069>.

In relation to the Laplace transitions described in section C.3.1, this update a) produces pairs that correspond to transitions observed in real data and b) allows for smooth transitions by defining the data generation process as opposed to being limited by the given collected dataset (e.g. dSprites). We generate the data online, thus training the model to fit the underlying distribution as opposed to a sampled finite dataset.

However, as noted previously, all supervised metrics aggregated in DisLib are inapplicable to continuous factors, which is problematic as the generating distribution is effectively continuous with respect to a subset of the factors. Therefore, we limit our quantitative evaluation to MCC for continuous datasets. Additionally, as mentioned above, to evaluate disentanglement with the standard metrics, we bin the collected transition statistics to match the size of dSprites and use the set of bin centers as the new set of values. The details of which are in Table 7, note that the discretization corresponds to the scale of the dSprites factor set.

C.3.4 KITTI MOTS Pedestrian Masks

While Natural Sprites enables evaluation of disentanglement with natural transitions, we note that the disentanglement framework which requires knowledge of the underlying generative factors is unrealistic for real-world data. As we state in the introduction, the assumption that a visual representation of the world can be constructed via a generative process that receives factors of variation as input and produces natural signals as output is not true in the literal sense. Measurements such as scale and position correspond to object properties that are ecologically relevant to the observer and can serve as suitable alternatives to the typical generative factors. We directly test this using our KITTI Masks dataset.

To create the dataset, we download annotations from the Multi-Object Tracking and Segmentation (MOTS) Evaluation Benchmark [19–21], which is split into KITTI MOTS and MOTSChallenge⁵. Both datasets contain sequences of pedestrians with their positions densely annotated in the time and pixel domains. The original image sizes are 1080×1920 or 480×640 resolution for MOTSChallenge and between 370 and 374 pixels tall by 1224 and 1242 pixels wide for KITTI MOTS. For simplicity, we only consider the instance segmentation masks for pedestrians and do not use the raw data. We use nearest neighbor down-sampling for each frame such that the height was 64 pixels and the width is set to conserve the aspect ratio. After down-sampling, we use a horizontal sliding window approach to extract six equally spaced windows of size 64×64 (with overlap) for each sequence in both datasets. Note that here we make reasonable assumptions on horizontal translation and scale invariance of the dataset. We justify the assumed scale invariance by observing that the data is collected from a camera mounted onto a car which has varying distance to pedestrians. To confirm the translation invariance, we show an ablation study on the number of horizontal images. Instead of six horizontal,

⁵<https://www.vision.rwth-aachen.de/page/mots>

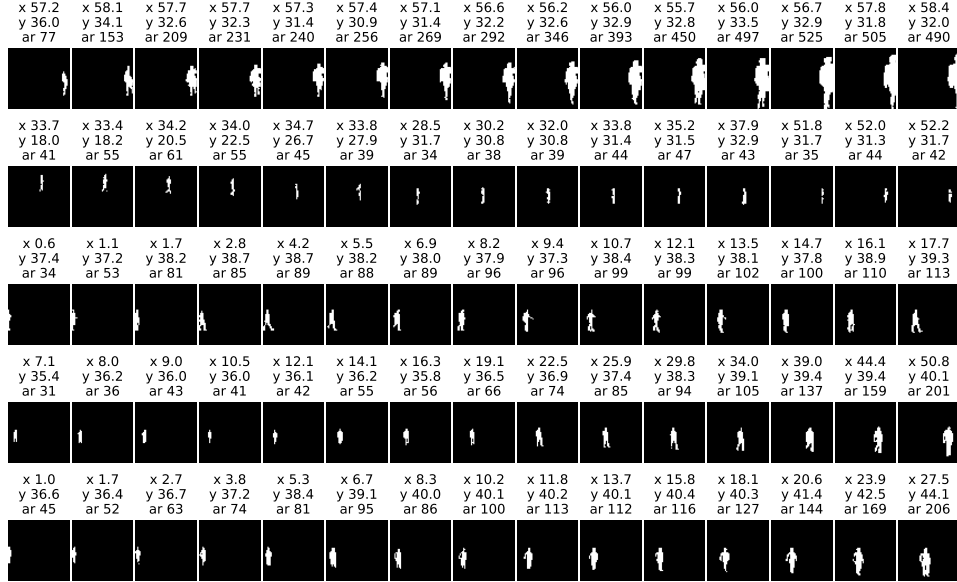


Figure 6: KITTI Masks : Each row corresponds to sequential frames from random sequences in the KITTI-Mssks dataset. Above each image we denote measured object properties where x, y correspond to the center of mass position and ar corresponds to the area.

equally spaced sliding windows, we only use two which leads to differently placed windows. We do not observe significant changes in the reported data statistics (e.g. the kurtosis of the fit stays within $\pm 10\%$ of the previous value for Δx transitions). The values of Δy and $\Delta area$ do not change significantly compared to Table 8.

For each resulting $64 \times 64 \times T$ sequence, where T denotes the number of time steps in the sequence, we extract all individual pedestrian masks based on their object instance identity and create a new sequence for each pedestrian such that each resulting sequence only contains a single pedestrian. We ignore images with masks that have less than 30 pixels as they are too far away or occluded and not recognizable by humans. We keep all sequences of two or more frames, as the algorithm only requires pairs of frames for training.

The resulting **KITTI Masks** dataset consists of 2,120 sequences of individual pedestrians with lengths between 2 and 710 frames each, resulting in a total of 84,626 individual frames. We estimate ground truth factors by calculating the x and y coordinates of the center of mass of each pedestrian in each frame and the area (number of pixels in mask). We leave the Δt between time frames within a pair as a hyperparameter, and test $\Delta t = 1$ and $\Delta t = 5$ as described in the main paper. During training, we augment the data by applying horizontal and vertical translations of ± 5 pixels and rotations of $\pm 2^\circ$ degree. We apply the exact same data augmentation to both images within a pair to not change any transition statistics. For samples and the corresponding ground truth factors see Fig. 6. The benchmark is available at <https://zenodo.org/record/3931823>.

D Additional Results

D.1 Extended Data Analysis

We report the empirical estimates of Kurtosis in Table 8. We report the log-likelihood scores for the Δ area, Δx , Δy statistics in Tables 9, 10, and 11, respectively for a Normal, a Laplace and a generalized Laplace/Normal distribution. For these distributions, we also report the fit parameters for the Δ area, Δx , Δy statistics in Tables 12, 13, and 14, respectively, where the shape parameter α of the generalized Laplacian is bolded. As a higher likelihood indicates a better fit, we can see further evidence that natural transitions are highly leptokurtic; a Laplace distribution ($\alpha = 1$) is a better fit than a Gaussian ($\alpha = 2$), while the generalized Laplacian yields the highest likelihood consistently with $\alpha \approx 0.5$ for all measurements, as indicated in the main paper.

| dataset | N | Δ area | Δ x | Δ y |
|---------|--------|---------------|------------|------------|
| KITTI | 82506 | 68.92 | 38.50 | 65.39 |
| YouTube | 234652 | 76.49 | 39.98 | 35.59 |

Table 8: Empirical estimates of Kurtosis for mask transitions per metric for each dataset.

| dataset | N | genlaplace | normal | laplace |
|---------|--------|------------|-----------|-----------|
| KITTI | 82506 | -3.21e+05 | -3.79e+05 | -3.35e+05 |
| YouTube | 234652 | -1.29e+06 | -1.45e+06 | -1.33e+06 |

Table 9: Maximum likelihood scores for the considered distributions on Δ area for each dataset.

| dataset | N | genlaplace | normal | laplace |
|---------|--------|------------|-----------|-----------|
| KITTI | 82506 | -8.72e+04 | -1.20e+05 | -9.25e+04 |
| YouTube | 234652 | -4.50e+05 | -5.64e+05 | -4.74e+05 |

Table 10: Maximum likelihood scores for the considered distributions on Δ x for each dataset.

| dataset | N | genlaplace | normal | laplace |
|---------|--------|------------|-----------|-----------|
| KITTI | 82506 | -7.59e+04 | -1.07e+05 | -7.86e+04 |
| YouTube | 234652 | -4.40e+05 | -5.45e+05 | -4.60e+05 |

Table 11: Maximum likelihood scores for the considered distributions on Δ y for each dataset.

| dataset | N | genlaplace | normal | laplace |
|---------|--------|--------------------------------|----------------------|----------------------|
| KITTI | 82506 | [4.55e-01, 1.00e+00, 1.01e+00] | [4.53e-01, 2.39e+01] | [1.00e+00, 1.07e+01] |
| YouTube | 234652 | [4.44e-01, 1.47e-16, 5.04e+00] | [2.25e-01, 1.16e+02] | [7.73e-09, 5.28e+01] |

Table 12: Parameter fits for the considered distributions on Δ area for each dataset. The parameters are (alpha, location, rate) for generalized Laplace/Normal, (location, rate) for the other two distributions.

| dataset | N | genlaplace | normal | laplace |
|---------|--------|--------------------------------|----------------------|----------------------|
| KITTI | 82506 | [5.87e-01, 4.76e-02, 1.69e-01] | [5.34e-02, 1.04e+00] | [5.49e-02, 5.64e-01] |
| YouTube | 234652 | [5.15e-01, 1.15e-14, 2.57e-01] | [2.32e-03, 2.68e+00] | [7.54e-09, 1.38e+00] |

Table 13: Parameter fits for the considered distributions on Δ x for each dataset. The parameters are (alpha, location, rate) for generalized Laplace/Normal, (location, rate) for the other two distributions.

| dataset | N | genlaplace | normal | laplace |
|---------|--------|--------------------------------|----------------------|----------------------|
| KITTI | 82506 | [6.94e-01, 1.02e-02, 2.32e-01] | [3.84e-02, 8.86e-01] | [1.71e-02, 4.77e-01] |
| YouTube | 234652 | [5.48e-01, 2.93e-13, 3.08e-01] | [8.81e-03, 2.47e+00] | [9.15e-04, 1.30e+00] |

Table 14: Parameter fits for the considered distributions on Δ y for each dataset. The parameters are (alpha, location, rate) for generalized Laplace/Normal, (location, rate) for the other two distributions.

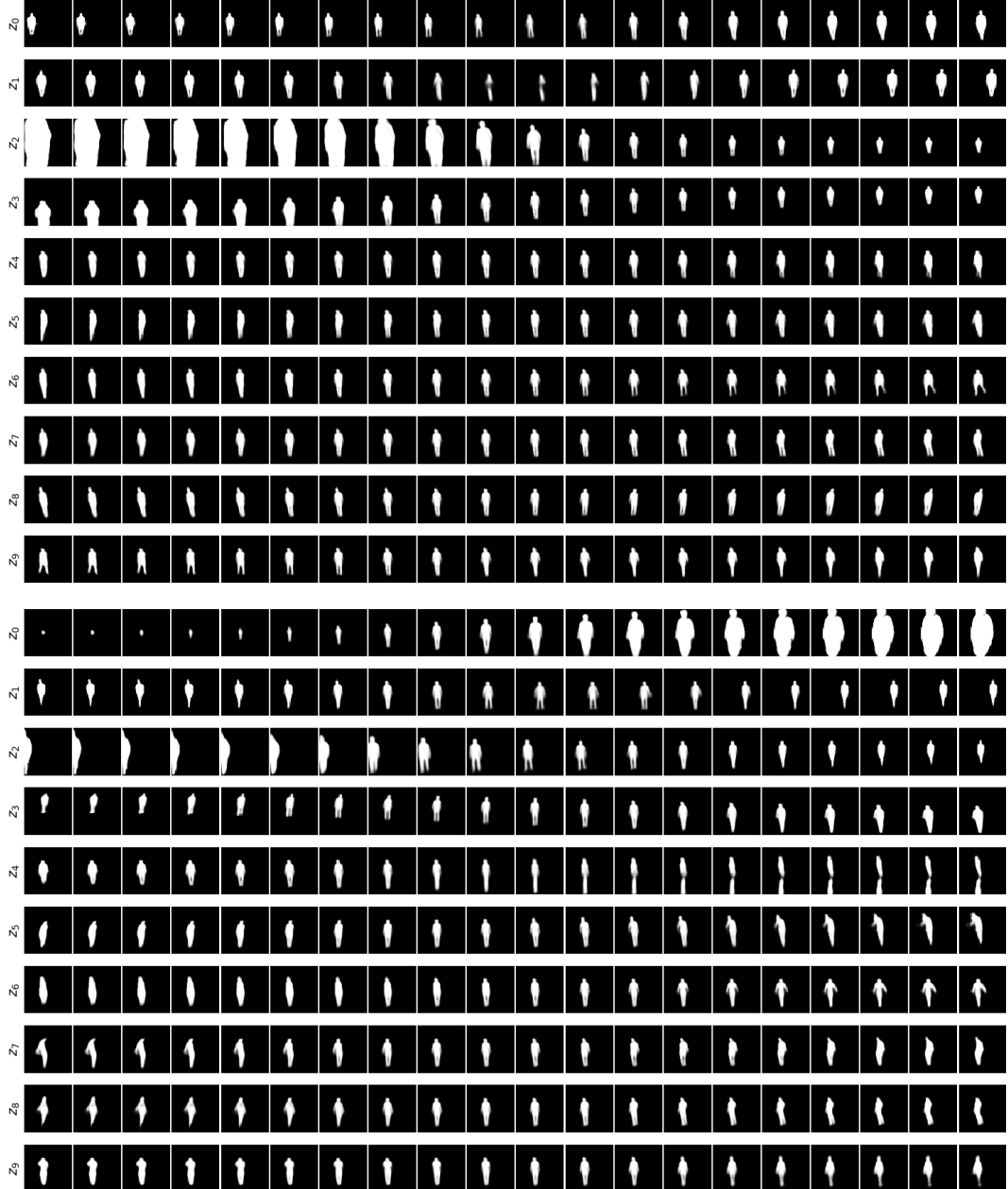


Figure 7: **KITTI Masks Latent Representations.** We show axis latent traversals along each dimension for the β -VAE (top) and SlowVAE (bottom). Here, the latents z_i are sorted from top to bottom in ascending order according to the mean variance output of the encoder. With MCC correlation (see e.g. Fig. 13) the known ground truth factors are matched as following: β -VAE: scale $\sim z_2$, x-position $\sim z_1$ and y-position $\sim z_3$; SlowVAE: scale $\sim z_0$, x-position $\sim z_1$ and y-position $\sim z_3$. With these latent visualizations alone, there is no significant difference visible between β -VAE and SlowVAE. However, we see a quantitative difference with the MCC score (see Table 5) and a qualitative difference when directly observing latent embeddings (see Fig. 13).

D.2 All DisLib Results

We include results on all DisLib datasets, dSprites [47], Cars3D [48], SmallNORB [49], Shapes3D [50], MPI3D [51], in Tables 15, 16, 17, 18, and 19, respectively. We report both median (a.d.) to compare to the previous median scores reported in [10], as well as the the more common mean (s.d.) scores for future comparisons and straightforward statistical estimates of significant differences between models.

| Model (Data) | BetaVAE | FactorVAE | MIG | DCI | Modularity | SAP |
|--------------------------------|-------------|-------------|-------------|------------|------------|-----------|
| β -VAE (<i>i.i.d.</i>) | 82.3 | 66.0 | 10.2 | 18.6 | 82.2 | 4.9 |
| Ada-ML-VAE (LOC) | 89.6 | 70.1 | 11.5 | 29.4 | 89.7 | 3.6 |
| Ada-GVAE (LOC) | 92.3 | 84.7 | 26.6 | 47.9 | 91.3 | 7.4 |
| SlowVAE (LOC) | 89.7 (3.8) | 81.4 (8.4) | 34.5 (9.6) | 50.0 (6.9) | 87.1 (2.0) | 5.1 (1.5) |
| SlowVAE (LAP) | 100.0 (0.0) | 99.2 (2.3) | 28.2 (8.2) | 65.5 (3.1) | 96.8 (1.4) | 6.0 (2.4) |
| SlowVAE (LOC) | 87.0 (5.1) | 75.2 (11.1) | 28.3 (11.5) | 47.7 (8.5) | 86.9 (2.8) | 4.4 (2.0) |
| SlowVAE (LAP) | 100.0 (0.0) | 97.5 (3.0) | 29.5 (9.3) | 65.4 (3.6) | 96.5 (1.6) | 8.1 (3.0) |

Table 15: **DSprites**. Median and absolute deviation (a.d.) metric scores across 10 random seeds (first three rows are from [10]). Bottom two rows give mean and standard deviation (s.d.) for the models presented in this paper.

| Model (Data) | BetaVAE | FactorVAE | MIG | DCI | Modularity | SAP |
|--------------------------------|-------------|------------|------------|------------|------------|-----------|
| β -VAE (<i>i.i.d.</i>) | 100.0 | 87.9 | 8.8 | 22.5 | 90.2 | 1.0 |
| Ada-ML-VAE (LOC) | 100.0 | 87.4 | 14.7 | 45.6 | 94.6 | 2.8 |
| Ada-GVAE (LOC) | 100.0 | 90.2 | 15.0 | 54.0 | 93.9 | 9.4 |
| SlowVAE (LOC) | 100.0 (0.0) | 90.4 (0.4) | 15.7 (1.5) | 48.9 (1.7) | 95.7 (1.0) | 1.6 (0.4) |
| SlowVAE (LAP) | 100.0 (0.0) | 91.0 (2.5) | 9.7 (1.1) | 51.0 (2.2) | 94.4 (1.1) | 1.7 (0.9) |
| SlowVAE (LOC) | 100.0 (0.0) | 90.4 (0.5) | 15.4 (2.2) | 48.0 (2.4) | 95.4 (1.5) | 1.6 (0.5) |
| SlowVAE (LAP) | 100.0 (0.0) | 90.2 (3.5) | 10.4 (1.8) | 50.9 (2.7) | 94.1 (1.2) | 2.0 (1.1) |

Table 16: **Cars3D**. Median and absolute deviation (a.d.) metric scores across 10 random seeds (first three rows are from [10]). Bottom two rows give mean and standard deviation (s.d.) for the models presented in this paper.

| Model (Data) | BetaVAE | FactorVAE | MIG | DCI | Modularity | SAP |
|--------------------------------|------------|------------|------------|------------|------------|-----------|
| β -VAE (<i>i.i.d.</i>) | 74.0 | 49.5 | 21.4 | 28.0 | 89.5 | 9.8 |
| Ada-ML-VAE (LOC) | 91.0 | 72.1 | 31.1 | 34.1 | 86.1 | 15.3 |
| Ada-GVAE (LOC) | 87.9 | 55.5 | 25.6 | 33.8 | 78.8 | 10.6 |
| SlowVAE (LOC) | 85.4 (2.2) | 54.7 (1.6) | 24.9 (1.3) | 31.8 (0.5) | 86.5 (3.3) | 6.3 (0.7) |
| SlowVAE (LAP) | 87.4 (0.5) | 74.0 (1.5) | 27.8 (0.8) | 42.4 (0.6) | 97.7 (0.7) | 8.2 (1.1) |
| SlowVAE (LOC) | 85.0 (2.9) | 54.9 (2.0) | 24.6 (1.7) | 31.9 (0.6) | 85.3 (4.1) | 6.3 (0.8) |
| SlowVAE (LAP) | 87.1 (0.7) | 73.4 (1.7) | 28.1 (1.0) | 42.4 (0.7) | 97.3 (0.8) | 7.5 (1.3) |

Table 17: **SmallNORB**. Median and absolute deviation (a.d.) metric scores across 10 random seeds (first three rows are from [10]). Bottom two rows give mean and standard deviation (s.d.) for the models presented in this paper.

D.3 Latent Space Visualizations

We visualize differences in learned latent representations using image embedding in Figures 8- 21. We show four different plots for each dataset considered and include all available models. Each figure corresponds to a different dataset.

In Figures 8- 14 we display the mean correlation coefficient matrix and the latent representations for each ground-truth, as described in the main text for Fig. 4.

| Model (Data) | BetaVAE | FactorVAE | MIG | DCI | Modularity | SAP |
|--------------------------------|-------------|------------|-------------|------------|------------|-----------|
| β -VAE (<i>i.i.d.</i>) | 98.6 | 83.9 | 22.0 | 58.8 | 93.8 | 6.2 |
| Ada-ML-VAE (LOC) | 100.0 | 100.0 | 50.9 | 94.0 | 98.8 | 12.7 |
| Ada-GVAE (LOC) | 100.0 | 100.0 | 56.2 | 94.6 | 97.5 | 15.3 |
| SlowVAE (LOC) | 100.0 (0.1) | 97.3 (4.0) | 64.4 (8.4) | 82.6 (4.4) | 95.5 (1.6) | 5.8 (0.9) |
| SlowVAE (LAP) | 100.0 (0.0) | 95.9 (2.6) | 62.5 (3.1) | 85.6 (4.0) | 98.1 (0.6) | 8.2 (1.7) |
| SlowVAE (LOC) | 99.9 (0.3) | 95.4 (5.2) | 58.8 (13.0) | 82.3 (5.4) | 95.2 (2.0) | 5.7 (1.4) |
| SlowVAE (LAP) | 100.0 (0.0) | 95.0 (3.2) | 61.5 (4.5) | 85.0 (4.7) | 98.3 (0.8) | 8.9 (2.6) |

Table 18: **Shapes3D**. Median and absolute deviation (a.d.) metric scores across 10 random seeds (first three rows are from [10]). Bottom two rows give mean and standard deviation (s.d.) for the models presented in this paper.

| Model (Data) | BetaVAE | FactorVAE | MIG | DCI | Modularity | SAP |
|--------------------------------|------------|------------|------------|------------|------------|------------|
| β -VAE (<i>i.i.d.</i>) | 54.6 | 32.2 | 7.2 | 19.5 | 87.4 | 3.7 |
| Ada-ML-VAE (LOC) | 72.6 | 47.6 | 24.1 | 28.5 | 87.5 | 7.4 |
| Ada-GVAE (LOC) | 78.9 | 62.1 | 28.4 | 40.1 | 91.6 | 21.5 |
| SlowVAE (LOC) | 70.9 (3.5) | 47.2 (2.8) | 37.4 (8.0) | 35.2 (1.3) | 88.9 (1.0) | 10.7 (1.2) |
| SlowVAE (LAP) | 87.2 (2.9) | 67.3 (6.2) | 26.1 (2.9) | 44.4 (2.1) | 91.1 (1.4) | 21.3 (2.1) |
| SlowVAE (LOC) | 71.6 (4.4) | 48.7 (3.7) | 29.7 (9.8) | 34.6 (1.7) | 88.4 (1.3) | 10.9 (1.5) |
| SlowVAE (LAP) | 86.5 (3.5) | 65.5 (8.3) | 26.9 (3.1) | 44.9 (2.6) | 91.2 (1.7) | 19.9 (4.7) |

Table 19: **MPI3D**. Median and absolute deviation (a.d.) metric scores across 10 random seeds (first three rows are from [10]). Bottom two rows give mean and standard deviation (s.d.) for the models presented in this paper.

The top row is the sorted absolute correlation coefficient matrix between the latents (rows) and the ground truth generating factors (columns). The latent dimensions are permuted such that the sum on the diagonal is maximal. This is achieved by an optimal, non-greedy matching process for each ground truth factor with its corresponding latent, as described in appendix B. As such, a more prevalent diagonal structure corresponds to a better mapping between the ground-truth factors and latent encoding.

The middle set of plots are latent embeddings of random training data samples. The y-axis denotes the ground truth generating factor and the x-axis denotes the corresponding latent factor as matched according to the main diagonal of the correlation matrix. For each dataset, we further color-code the latents by a categorical variable as denoted in each figure.

The bottom set of plots show the ground truth encoding compared to the second best latent as opposed to the diagonally matched latent. This plot can be used to judge how much the correspondence between latents is one-to-one or rather one-to-many.

To further investigate the latent representations, we show a scatter plot over the best and second best latents in figures 15-21. Here, the color-coding is matched by the ground truth factor denoted in each row.

When comparing the correlation matrix with the corresponding scatter plots, one can see that embeddings with sinusoidal curves have low correlation, which illustrates a shortcoming of the metric. Another limitation is that categorical variables which have no natural ordering have an order-dependent MCC score, indicating the permutation variance of MCC. With SlowVAE, we can infer three different types of embeddings. First, we have simple ordered ground truth factors with non-circular boundary conditions. Here, SlowVAE models often show a clear one-to-one correspondence (e.g. Fig 15 scale, x-position and y-position; Fig 18 θ -rotation; Fig 19 Φ -rotation). Second, we observe circular embeddings due to boundary conditions for certain factors (e.g. Fig 8, 15 3rd row; Fig 9, 16 2nd row). Note that not all datasets with orientations exhibit full rotations and thus do not have circular boundary conditions, e.g. smallNORB. Finally, we have categorical variables, where no order exists (e.g. Fig. 9, 16 top row, Fig 10, 17 top row, Fig 11, 18 top row) resulting in separated but not necessarily ordered clusters.

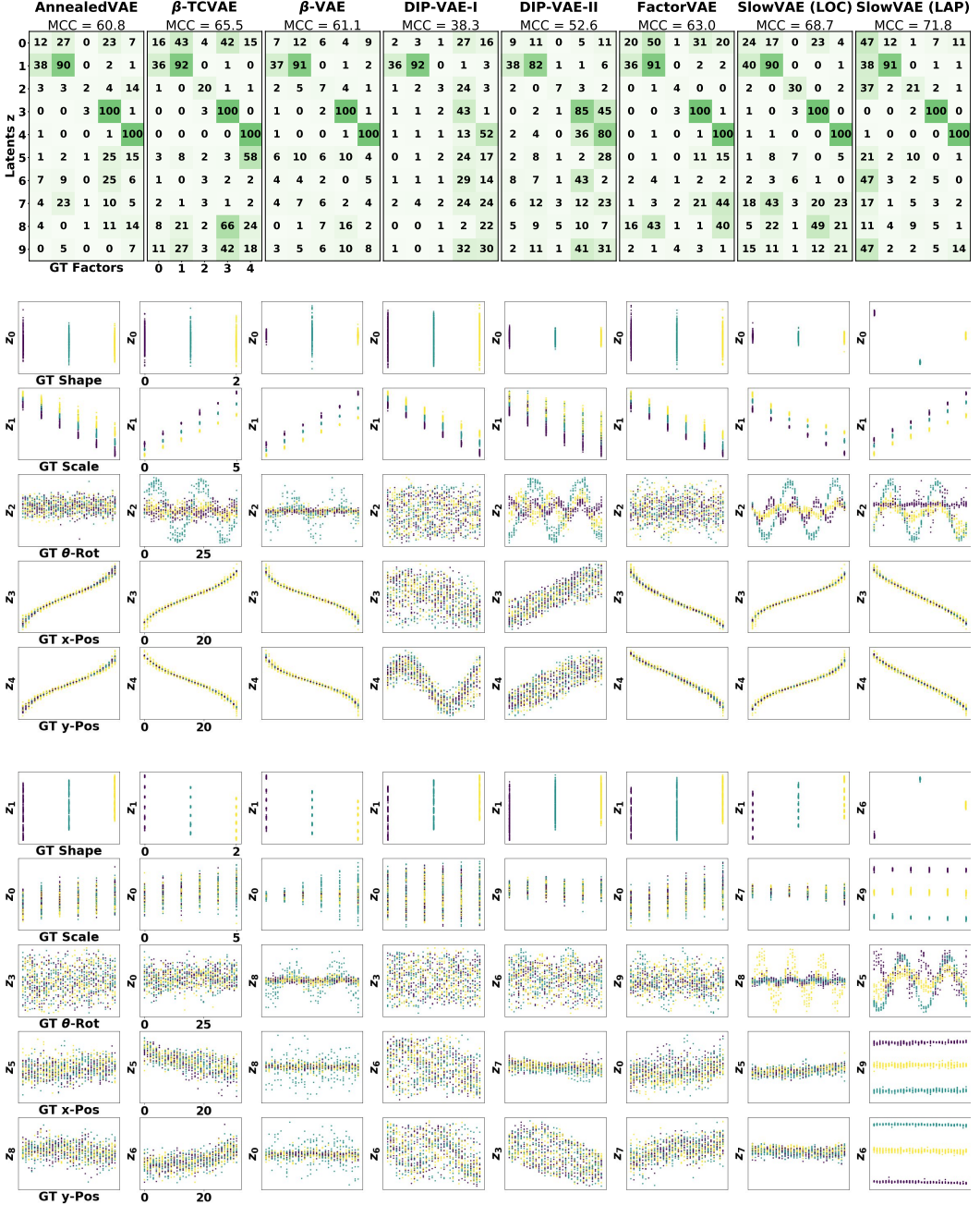


Figure 8: **DSprites Latent Representations.** Top, MCC correlation matrices. Middle five rows, model latent over highest correlating ground truth factor. Bottom five rows, model latent over second highest correlating ground truth factor. The color-coding corresponds to the shapes: heart/yellow, ellipse/turquoise and square/purple.

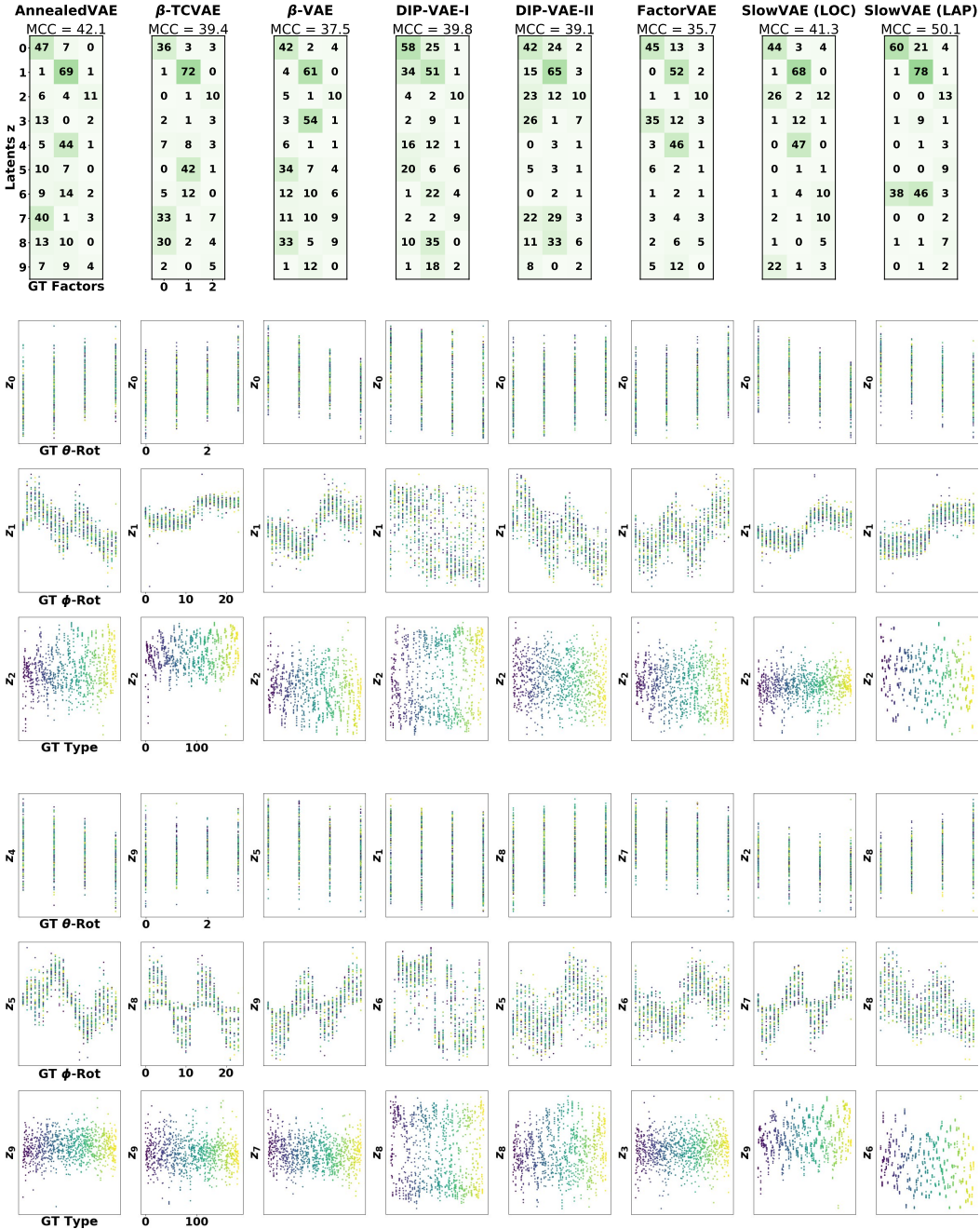


Figure 9: **Cars3D Latent Representations.** Top, MCC correlation matrices. Middle three rows, model latent over highest correlating ground truth factor. Bottom three rows, model latent over second highest correlating ground truth factor. The color-coding corresponds to the 183 different car types (GT Types) in the dataset.

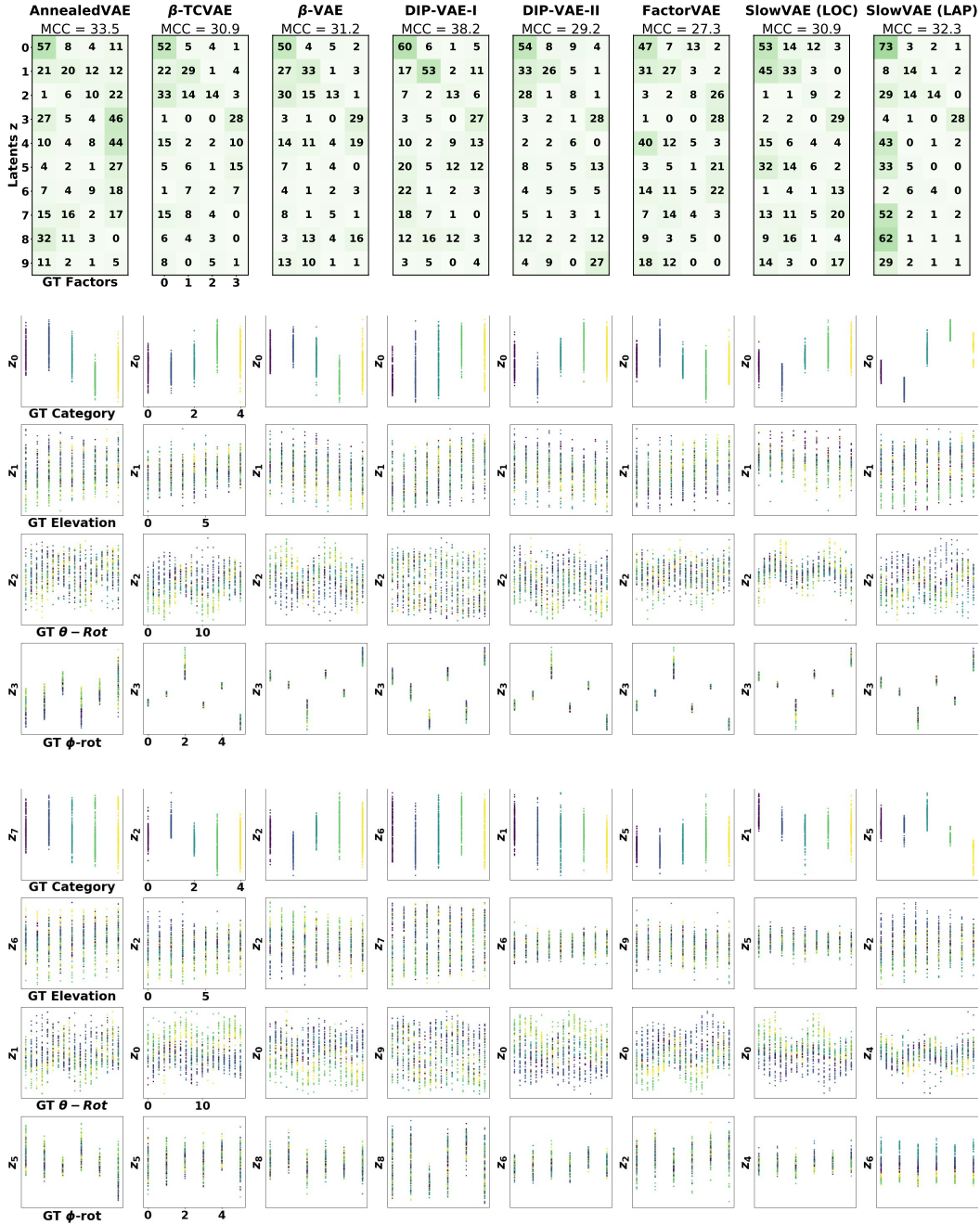


Figure 10: **SmallNorb Latent Representations.** Top, MCC correlation matrices. Middle four rows, model latent over highest correlating ground truth factor. Bottom four rows, model latent over second highest correlating ground truth factor. The color-coding corresponds to the five different GT categories in the dataset.

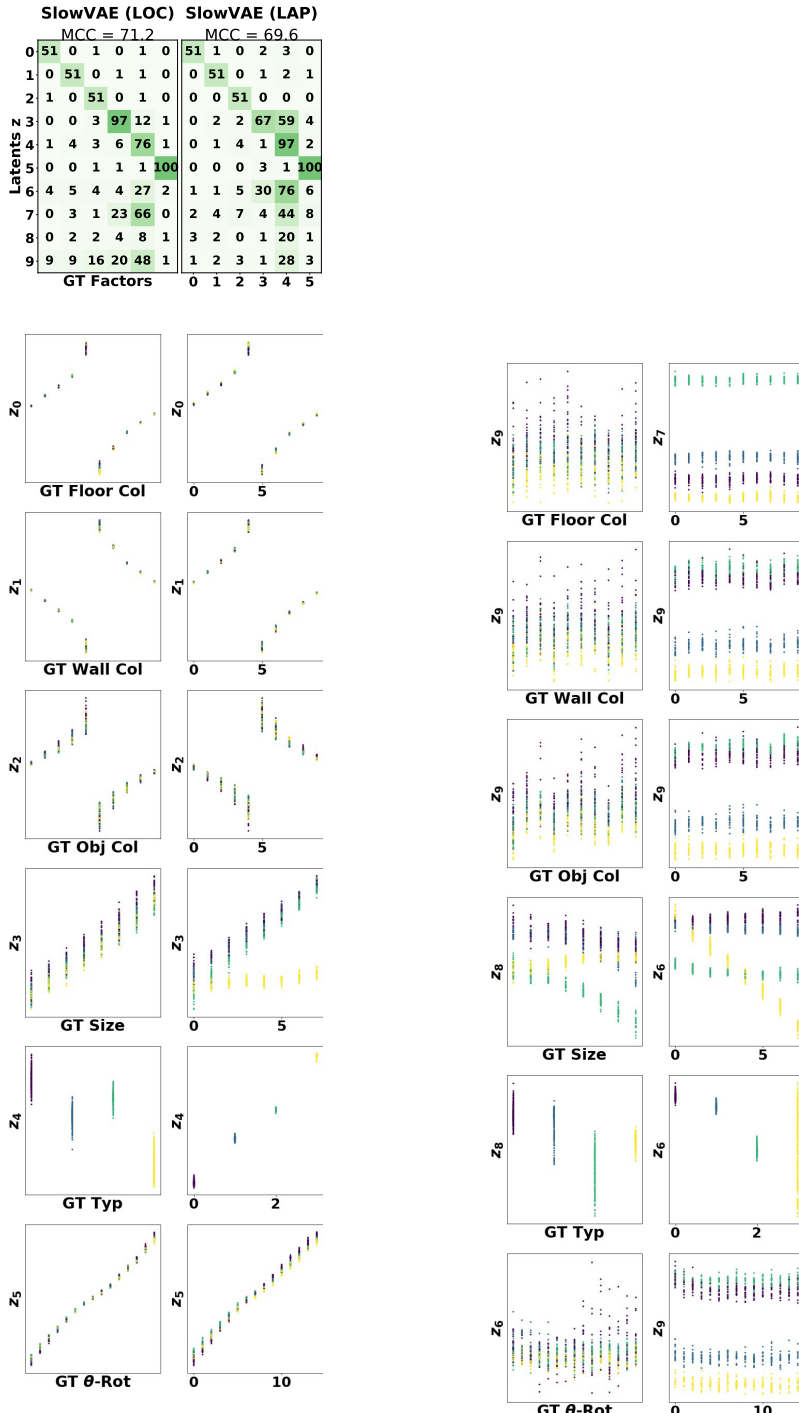


Figure 11: **Shapes3D Latent Representations.** Top, MCC correlation matrices. Left two columns, model latent over highest correlating ground truth factor. Right two columns, model latent over second highest correlating ground truth factor. The color-coding corresponds to the four different object types (GT-Type) in the dataset.

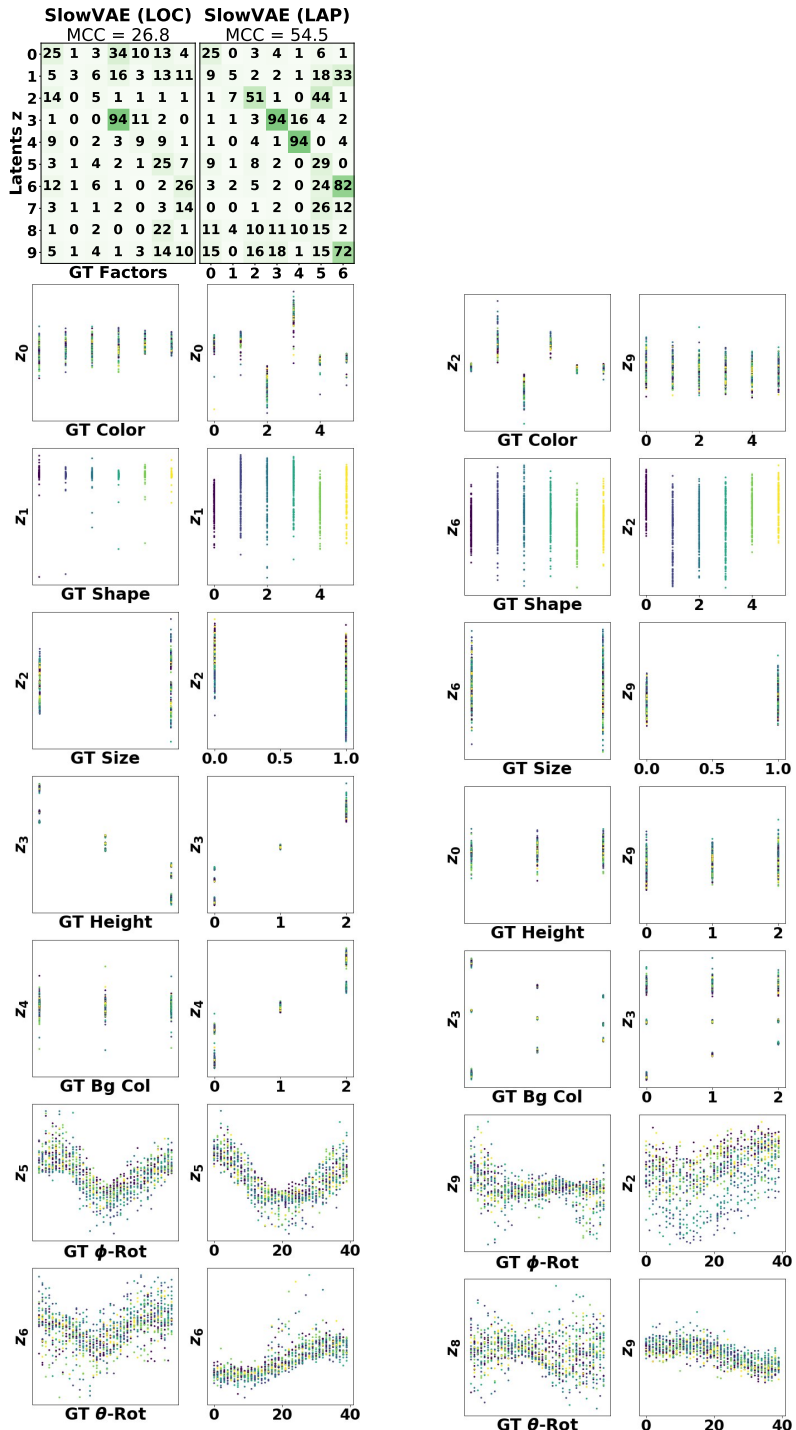


Figure 12: **MPI3DReal Latent Representations**. Top, MCC correlation matrices. Left two columns, model latent over highest correlating ground truth factor. Right two columns, model latent over second highest correlating ground truth factor. The color-coding corresponds to the six different object shapes (GT Shape) in the dataset.

| β-VAE | | | SlowVAE | | |
|-------------------------------|----|----|----------------|----|----|
| | | | MCC = 90.7 | | |
| Latents z | | | GT Factors | | |
| 0 | 86 | 13 | 95 | 2 | 8 |
| 1 | 1 | 59 | 10 | 81 | 1 |
| 2 | 26 | 17 | 7 | 5 | 95 |
| 3 | 2 | 5 | 11 | 14 | 11 |
| 4 | 4 | 9 | 9 | 2 | 2 |
| 5 | 6 | 38 | 14 | 11 | 11 |
| 6 | 1 | 0 | 10 | 7 | 14 |
| 7 | 1 | 2 | 9 | 16 | 11 |
| 8 | 9 | 4 | 25 | 7 | 27 |
| 9 | 3 | 21 | 50 | 18 | 9 |

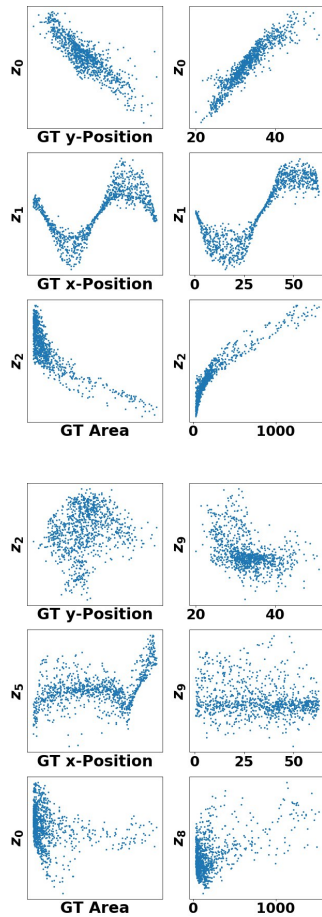


Figure 13: **KITTI Masks Latent Representations.** Top, MCC correlation matrices. Middle three rows, model latent over highest correlating ground truth factor. Bottom three rows, model latent over second highest correlating ground truth factor.

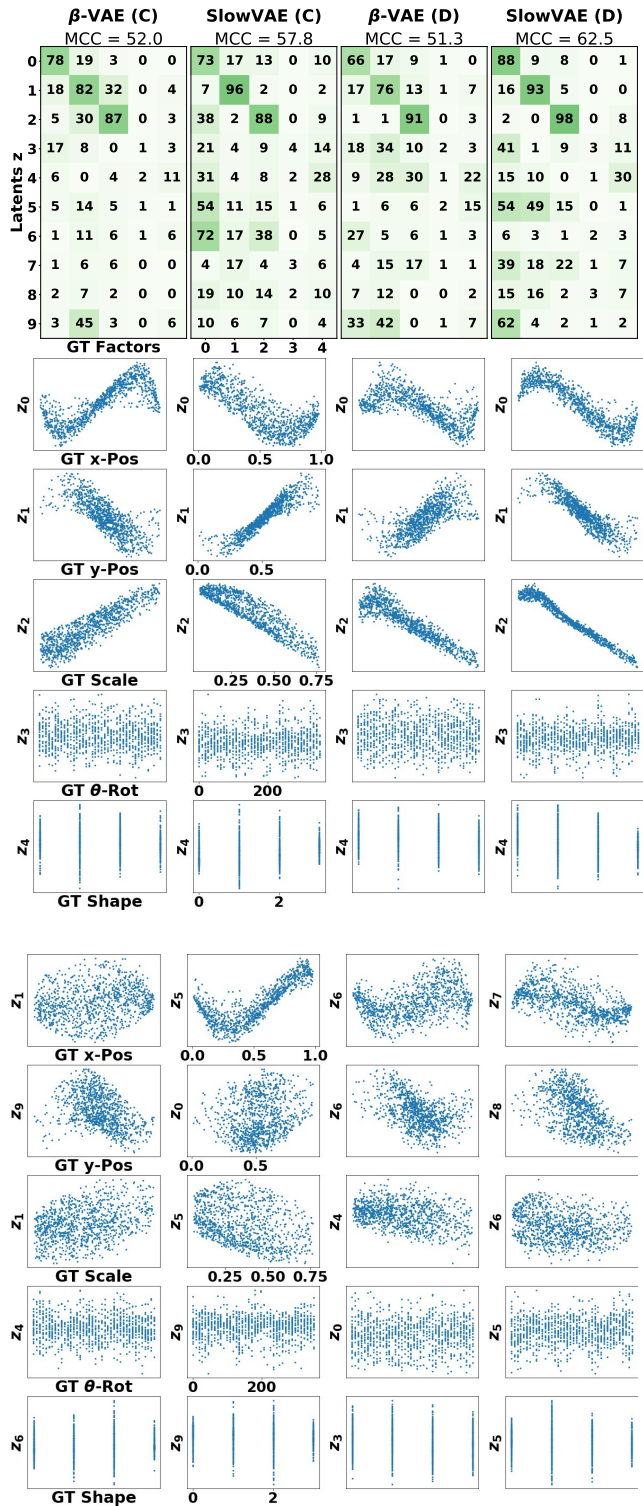


Figure 14: **Natural Sprites Latent Representations.** Top, MCC correlation matrices. Middle five rows, model latent over highest correlating ground truth factor (colored by category). Bottom five rows, model latent over second highest correlating ground truth factor. The left two columns denote the continuous (C) version of Natural Sprites, whereas the right two columns correspond to the discretized (D) version.

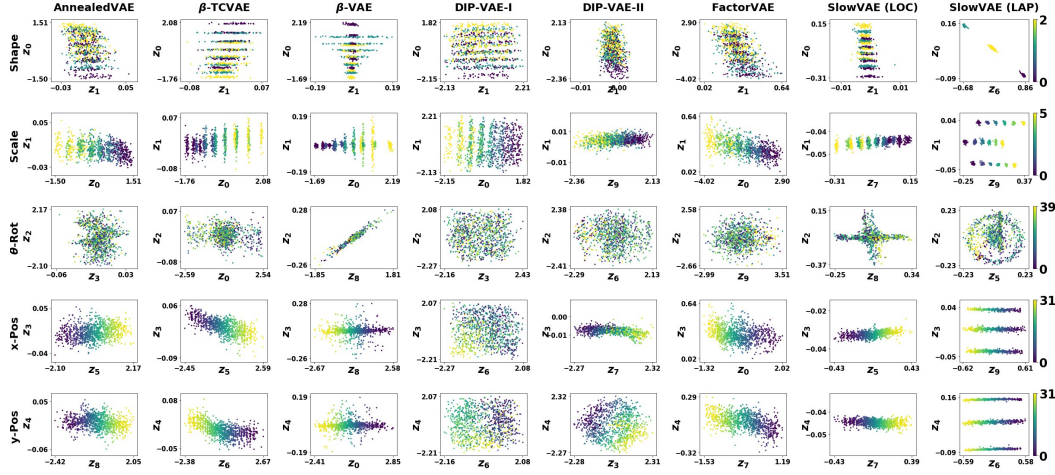


Figure 15: **DSprites Latent Representations.** Best two latents selected from Fig 8. Color-coded by the corresponding ground truth factor.

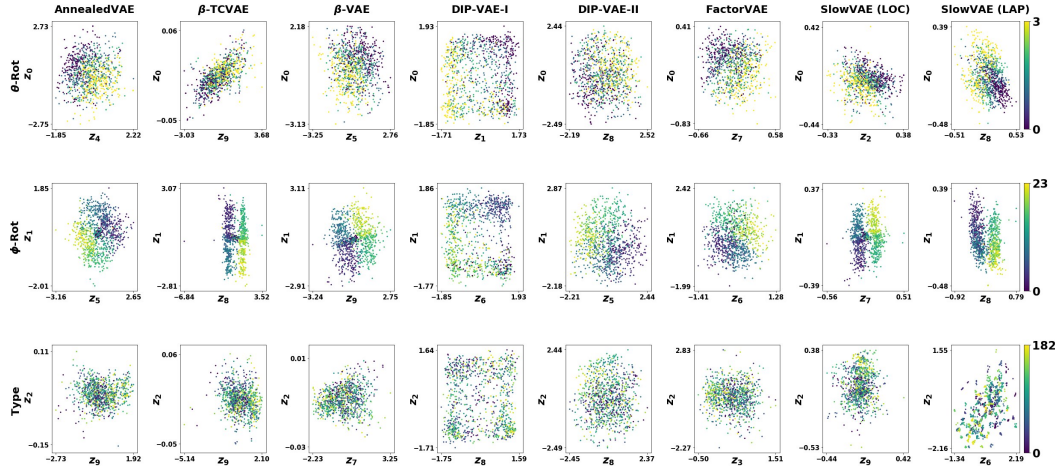


Figure 16: **Cars3D Latent Representations.** Best two latents selected from Fig 9. Color-coded by ground truth.

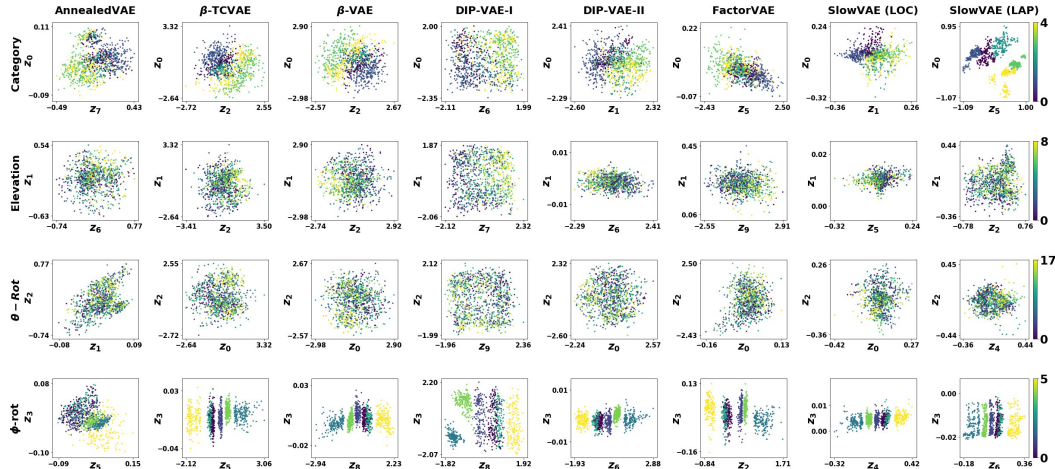


Figure 17: **SmallNorb Latent Representations.** Best two latents selected from Fig 10. Color-coded by ground truth.

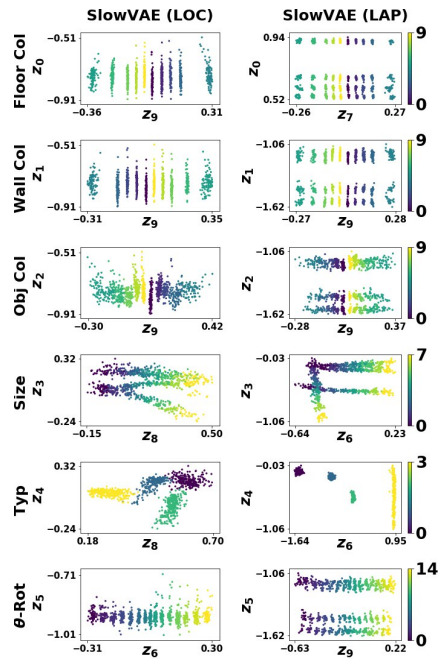


Figure 18: **Shapes3D Latent Representations**. Best two latents selected from Fig 11. Color-coded by ground truth.

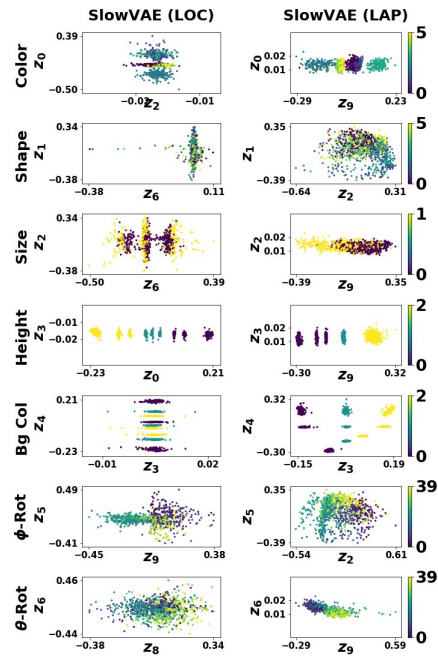


Figure 19: **MPI3DReal Latent Representations**. Best two latents selected from Fig 12. Color-coded by ground truth.

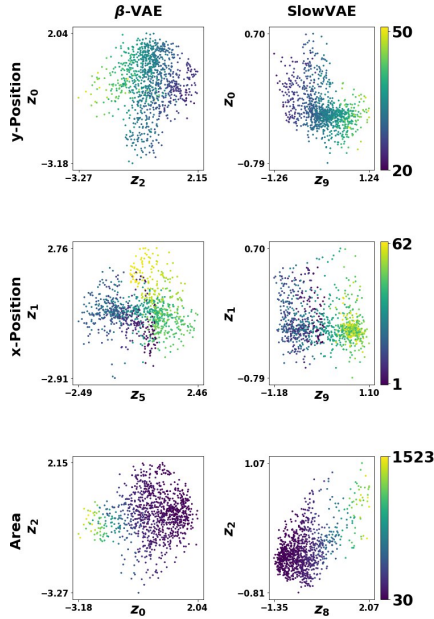


Figure 20: **KITTI Masks Latent Representations.** Best two latents selected from Fig 13. Color-coded by ground truth.

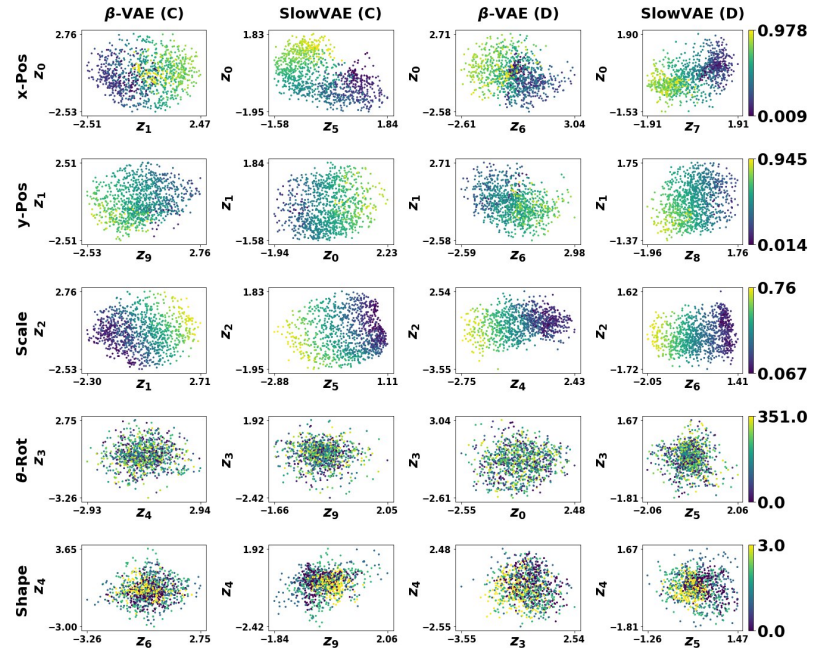


Figure 21: **Natural Sprites Masks Latent Representations.** Best two latents selected from Fig 14. The left two columns denote the continuous (C) version of Natural Sprites, whereas the right two columns correspond to the discretized (D) version. Color-coded by ground truth.